Pseudo two-dimensional modeling and validation of a hybrid rocket combustion chamber

Elena Quero Granado, Jouke Hijlkema, Jean-Yves Lestrade, Jérôme Anthoine

To cite this version:

Elena Quero Granado, Jouke Hijlkema, Jean-Yves Lestrade, Jérôme Anthoine. Pseudo two-dimensional modeling and validation of a hybrid rocket combustion chamber. Journal of Propulsion and Power, 2022, 38 (6), 10.2514/1.B38682 . hal-04047111

HAL Id: hal-04047111
https://hal.science/hal-04047111v1

Submitted on 27 Mar 2023

Pseudo 2-Dimensional Modeling and Validation of a Hybrid Rocket Combustion Chamber

Elena Quero Granado*, Jouke Hijlkema†, Jean-Yves Lestrade ‡ and Jérôme Anthoine§
ONERA/DMPE, University of Toulouse, F-31055 Toulouse-France

A pseudo 2-D model for the cylindrical combustion chamber of a hybrid rocket is developed in this article with the purpose of its integration in a system design tool used for engine predesign phases. A compromise of simplicity and accuracy is thus required. Integral transient boundary layer equations are included and coupled with the mass and energy balances at the fuel surface, where fuel pyrolysis is described by an Arrhenius law. Studies assessing the model in the non-reactive case provide satisfactory results regarding the description of the boundary layer. Concerning the hybrid case, the computed steady-state fuel regression rates are found to be in the low region of the reference values coming from semiempirical laws for several oxidizer/fuel couples and oxidizer mass fluxes, producing errors up to 50% for certain sources. The effect of mass flux and motor size is correctly simulated. Eventually, the whole engine operation is assessed through the comparison of the computed results with three experimental tests realized at our laboratory and using a 87.5% Hydrogen Peroxide/High-Density Polyethylene couple. Corresponding results lead to regression rate errors varying in a wide range (from 10 to 40%). Such differences, although high, remain acceptable for our engine predesign phase application.

Nomenclature

A_d = Arrhenius preexponential constant, m/s.

$a_{thermal}$ = Thermal diffusivity, m^2/s.

B = Blowing number.

C_f = Skin friction coefficient.

$C_{f0,D}$ = Skin friction coefficient in the developed region of the channel, without surface blowing.

c_F = Theoretical thrust coefficient on the ground.

c_p = Specific heat constant, J/kg/K.

Presented as Paper 2021-3495 at the AIAA Propulsion and Energy 2021 Forum, August 9-11, 2021, VIRTUAL EVENT.

*Ph.D. Candidate, Rocket Propulsion Laboratory Unit, Multi-Physics for Energetics Department, elena.quero_granado@onera.fr.

†Research Scientist, Rocket Propulsion Laboratory Unit, Multi-Physics for Energetics Department, jouke.hijlkema@onera.fr.

‡Research Scientist, Rocket Propulsion Laboratory Unit, Multi-Physics for Energetics Department, jean-yves.lestrade@onera.fr.

§Head of Multi-Physics for Energetics Department, jerome.anthoine@onera.fr, AIAA Senior Member.

D = Diameter of the fuel port, m.

D_{diff} = Diffusion coefficient, m^2/s.

E_a = Activation energy in the Arrhenius pyrolysis law, J/mol.

F = Thrust force generated by the propulsion system, N

G = Fuel mass flux, kg/m^2/s.

h_{conv} = Heat convection coefficient, W/m^2/K.

h_D = Mass diffusion coefficient, m/s.

h_t = Specific total enthalpy, J/kg.

k = Thermal conductivity, W/m/K.

L = Length of the fuel block, m.

Le = Lewis number.

M = Mach number.

N_{sp} = Total number of species in the gas flow.

P = Pressure, Pa.

Pr = Prandtl number.

$\dot{Q}_{rad}^{net}$ = Net radiation heat flux, W/m^2.

R = Radius of the fuel port, m.

R_g = Gas constant, J/kg/mol.

Re = Reynolds number.

r = Radial coordinate, reference to the chamber axis.

r_M = Oxidizer to fuel mass ratio.

S = Cross sectional area, m^2.

Sc = Schmidt number.

St = Stanton number.

T = Temperature, K.

t = Time, s.

u = Axial velocity component, m/s.

v = Radial velocity component, m/s.

x = Axial coordinate.

Y_k = Mass fraction of the species k.

y = Transversal coordinate in the Cartesian frame, reference to the chamber axis.

z = Shvab-Zeldovich scalar variable.

γ = Heat capacity ratio.

$\Delta H^0_{f,k}$ = Specific enthalpy of formation of the species k, J/kg.

ΔH_{pyr} = Specific enthalpy of pyrolysis of the fuel, J/kg.

δ = Boundary layer thickness, m.

δ^* = Displacement thickness, m.

η = Radial coordinate, reference at the fuel surface.

η_c = Combustion efficiency.

θ = Momentum thickness, m.

$\mathcal{M}_k$ = Molar mass of the species k, kg/mol.

ρ = Density, kg/m^3.

τ = Viscous stress term, N/m^2.

$\dot{\omega}_k$ = Production rate of species k at the fuel surface, kg/m^2/s.

Subscripts

amb = Evaluated at ambient conditions.

ch = Averaged values at the chamber.

e = External gas flow region.

end = Conditions at the end of the test.

f = Corresponding to the solid fuel.

g = Referenced to the gas.

hyb = Corresponding to the hybrid phase of the engine.

in = Inlet conditions.

out = Conditions at the exit of the nozzle.

ox = Referenced to the oxidizer.

pyr = Corresponding to fuel pyrolysis.

r = Fuel regression.

ref = Reference value.

s = Evaluated at the fuel surface.

th = Evaluated at the nozzle throat.

vap = Vaporization conditions.

x = Local value along the axis.

δ = Evaluated at the boundary layer region.

0 = Initial conditions.

I. Introduction

Hybrid rocket technology constitutes both a low-cost and a high-performance solution (theoretical vacuum specific impulse being superior to 300 s for certain couples) for a space propulsion system when compared with its rocket propulsion counterparts (liquid and solid), allowing to reduce the manufacturing and production costs while maintaining a great deal in safety and throttability. These advantages lead to the application of hybrid space propulsion systems for sounding rockets, small satellite launchers or even orbital propulsion systems [1]. This technology is characterized by the combustion of two propellants stored at different states of matter: generally, the oxidizer, stored at the liquid or gaseous state is introduced into the combustion chamber by an injection system, where the carburant is stored at the solid state. As a result of the high temperatures of the injected gases and the heat transfers with the solid, the fuel is pyrolyzed and evaporized. The mix of both reactants produces a chemical reaction governed by a turbulent diffusion flame that is situated at a certain distance above the fuel surface. Finally, the gas products resulting from the combustion are expelled through the nozzle, generating thus, the engine thrust.

The interest for the production and exploitation of this technology resides in the knowledge of the engine performances at different configurations / conditions. A way to characterize the behaviour of the engine dwells in the realization of experimental test campaigns. Nevertheless, the high costs implied have boosted the development of numerical models. Indeed, two-dimensional / three-dimensional (2-D / 3-D) Computational Fluid Dynamics (CFD) codes can allow the obtention of quite accurate results (averaged fuel regression rate errors inferior to 10%) in the simulation of the combustion process of hybrid rockets [2–4], being able to simulate combustion kinetics, turbulence transport and parietal injection precisely. Nevertheless, the large computing time thereof represents a substantial hindrance for their applicability during the engine predesign phases, in which the thrust and the specific impulse are the results of interest.

Several system design tools have been developed for this purpose, allowing the simulation of a full Hybrid Rocket Engine (HRE) in a rapid and simple way [5–7]. The final aim in the exploitation of such tools results in the implementation of optimization algorithms enabling to obtain the best HRE configuration that accomplishes the mission requirements (specified ΔV and total spacecraft mass, for example) while enhancing some engine characteristics like the payload mass, the thrust level, the nozzle expansion ratio, etc. Several authors [8–10] have already developed and validated codes like these, providing HRE designs that prove to be a better choice (implying smaller economical costs and better performances) compared with other existing bipropellant propulsion system designs. These tools implement 0-D models or very simplified 1-D models to describe the internal chamber physics, with the use of semiempirical expressions (through fit coefficients) to characterize the fuel pyrolysis, such as the one proposed by Marxman [11]. These kind of laws are, however, dependent on the geometry and the dimensions of the motor, as well as the Oxidizer / Fuel (O/F) couple employed to characterize them. This fact may reduce their applicability and extrapolation to other engine configurations or larger size motors.

A need arises to merge both aspects: the development of a simple but reliable model capable of reproducing the most important physics inside the combustion chamber of a HRE in a wide range of configurations, and the conception of a system design tool allowing to predict the behavior of the propulsive system during the operation of the engine. The goal would be to use this tool during the preliminary design studies of a HRE. Therefore, the maximal error allowed for this kind of application should not overpass 30% as long as a computation can be completed in some minutes. Eventually, this tool could implement an optimization algorithm that would select the best engine solution as regards to a certain number of parameters.

Thus, it seems necessary to achieve a specific kind of modeling that would combine the speed and the simplicity in the calculations with the precision required. An approximation of a 2-D model applied to a cylindrical chamber (shape of most HRE applications) based on the integration of the two-dimensional boundary layer (BL) equations and using an Arrhenius law to characterize fuel pyrolysis seems to fit best both requirements of complexity and accuracy. These integral BL methods have been used in literature before to simulate non-reactive flows [12–15]. They have proven to be less time-consuming in relation to a full Navier-Stokes solver while providing satisfactory results. Lestrade [16] applied this type of model to describe the steady flow inside the combustion chamber of a HRE for liquefying fuels, resulting to be a good method to predict the regression rates for high oxidizer fluxes ($G_{ox} \geq 150$ kg/m^2/s).

A full description of a HRE test simulating the initial non-reactive (oxidizer) and the ignition / combustion phases of the engine as well as the effect of the possible changes in the flow conditions occuring during the engine operation is searched. It is therefore chosen to use a transient formulation. Furthermore, the numerical algorithm of the code employed for the resolution of the coupled equations in the chamber needs to be modular, so that the system design tool is able to accomodate different engine configurations and to simulate either a specific element of the engine (tank, injector, catalyst, pipelines, etc.) or the complete propulsive system.

This article introduces and develops the aforementioned model and presents the necessary verification steps to proceed to a first validation phase of the obtained numerical results through the comparison with analytical solutions and experimental data of reference.

II. Mathematical Model

The model for the combustion chamber of a HRE that is presented in this article consists of an approximation of the two-dimensional equations of the flow: it is based on the integration of the fluid dynamics equations along the radial direction of the chamber, followed by the numerical computation of the resulting equations along the axial direction. This model, named pseudo 2-D, which may also be known as *1.5-D* [17–19], takes into consideration the information in the radial direction of the flow through empirical correlations (e.g.: radial profiles of the main variables retrieved from the experiments) at the same time that it solves the flow equations in the axial direction. This characteristic notably allows the reduction of the computational time.

In this model, the transient and compressible formulation of the equations is employed. Several hypothesis are applied to reduce the complexity of the physics of the problem, leading thus, to a rapid resolution of this one. All these simplifications are meant to be applied to classical combinations of O/F for HREs. In the first place, the injection of oxidizer into the chamber is considered to be axial, completely gaseous and generating a flow in a turbulent regime. Regarding the latter aspect, it is known that the transition between a laminar to a turbulent flow in a circular duct (shape of most HRE combustion chambers) occurs in the range of $2300 < Re < 10^4$ for a non-reactive boundary layer without blowing [20]. However, this transition happens at smaller Reynolds numbers when the boundary layer is exposed to evaporation phenomena or to blowing from the fuel surface [21]. Taking into account that typical Reynolds numbers (based in the inner diameter of the fuel block) for hybrid rockets are at least of 10^4 ($G \sim 10 - 100$ kg/m^2/s, $\mu \sim 10^{-5}$ N/m^{2}s and $D \sim 10$ mm for lab-scale engines to 100 mm or more for a larger launch scale propulsion application), the flow inside the combustion chamber can be considered to be fully turbulent. In relation to the thermal and dynamic boundary layers, because Prandtl and Lewis numbers are taken equal to unity for the sake of simplicity, these two are overlapped. This also implies that the molecular diffusion coefficient (D_{diff}) is the same for all the species in the flow.

As regards to the combustion process inside the chamber, we contemplate that the initiation of combustion happens at the same time along the axial direction of the chamber once the temperature of any point at the surface reaches the pyrolysis temperature of the material. Once the combustion begins, the flame produced by the chemical reaction is self-sustained until the end of the engine operation. An infinitely fast chemistry (equilibrium) assumption is made to describe the combustion process inside the chamber. Hence, the thickness of the reactive zone is regarded to be infinitely thin, and the flame is considered to take place at stoichiometric conditions. The thermodynamic data generated by the combustion process are obtained through a chemical equilibrium code developed by Gordon and McBride [22]. This code has also been employed before for a HRE problem [10, 23, 24], providing in general, good estimations about the temperature and the fuel regression rate values in the combustion chamber. In particular, combustion conditions are retrieved through a constant temperature-pressure problem, where the inputs are the molecular formulas of the reactants (oxidizer and pyrolyzed fuel) and their corresponding temperature, pressure and mass fractions. Results are retrieved for a chemical equilibrium composition by the minimization of the Gibbs energy of the ensemble of species contained in the program database. To reduce the size of the system of equations to be solved by our model and thus, the computing time, only the species CO_2 and H_2O have been considered as main products of the stoichiometric combustion. In the nozzle, the thermodynamic properties of the flow are obtained by the theoretical rocket performance problem resolution in Gordon and McBride's tool for an infinite area combustion chamber in function of the retrieved mass O/F ratio and pressure at the end of the combustion chamber.

During the fuel ablation process, only one gazeous species is produced (the gaseous fuel component) and no surface reactions other than pyrolysis are considered (oxidation, hydrolyse, etc.). Furthermore, because fuel regression rates (order of mm/s) are much smaller than velocity magnitudes of the flow (m/s), a quasi steady-equilibrium assumption concerning the exchanges at the fuel surface is made as a first approximation. Additionally, for simplicity, radiation fluxes are neglected while performing the thermal exchanges in the flow.

Eventually, concerning the modeling of the solid fuel block, the curvature effects in the formulation of the equations are neglected. In the computation process, each axial station, x_i, in which the combustion chamber is divided, has a size of Δx_i that is characterized by a constant radius, R_i, updated at every time step based on the instantaneous fuel regression rate at that position.

A. Formulation

The unfolding flow inside the duct of a HRE is subject to viscous near-wall effects that induce the formation of a BL at the solid surface. The development of this BL can follow two different configurations: a hydrodynamically and thermally developing flow configuration, where the BL is growing inside the channel; and a fully developed flow one, where the BL occupies the entire radius of the channel (R). A schematics of the flow for the model presented in this article is depicted in Fig. 1. Additionally, in our model, we consider that in the developing flow configuration, the flow is divided in two zones along the radial direction. The first one corresponds to the inviscid core flow region, where the thermodynamic and mechanical variables characterizing the flow (density, velocity, temperature) are considered to remain constant in the radial direction, thus depending only on the axial position. Related differential equations can be found in Sec. II.A.1. A control volume for an element of size dx corresponding to this zone is represented by *C.V. 1* in Fig. 1. The second zone of the developing flow configuration is adjacent to the core flow region, and corresponds to the boundary layer, whose characteristic thickness (δ) is defined as the distance normal to the wall where the velocity of the flow has reached its streamwise value, u_e. In this zone, the viscous effects along the wall are accounted for. The corresponding control volume for an element of size dx is defined as *C.V. 2* in the same figure. Both control volumes, C.V. 1 and C.V. 2, forming the invsicid and viscous regions, respectively, are coupled through the boundary condition at the BL edge. More detail regarding this coupling will be given in Secs.II.A.1 and II.A.2, where equations for both regions are developed. The fully developed flow configuration corresponds to an established Poiseuille flow. In this case, no core flow is present and only one control volume over the radial direction (*C.V. 3* in Fig. 1) is defined for an infinitesimal element. Here, the dynamic and thermal BLs merge with the symmetry axis. As the equations describing this region correspond to the same BL equations of the C.V. 2, but integrated throughout the radius of the channel instead of the boundary layer thickness, these ones will not be presented in this article.

1. Integral core flow Equations

The core flow equations are defined from the unsteady, inviscid form of the fluid dynamics equations. The pseudo 2-D equations of continuity, momentum, energy and mass fractions are obtained by integrating the 2-D Euler equations [25] with respect to the coordinate r, normal to the fuel surface, over the thickness of the core flow region ($0 \leq r \leq R-\delta$). By employing the Leibnitz integral rule, the integrals of the partial derivatives in the different equations are expressed in

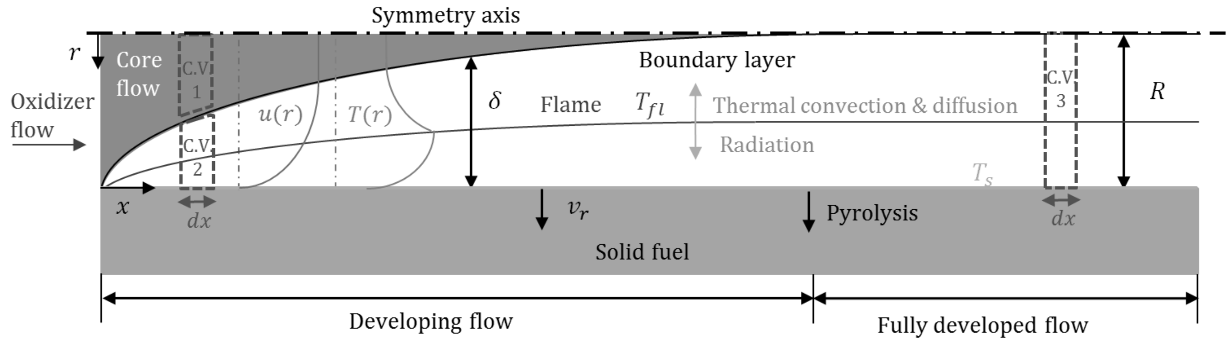

Fig. 1 Representation of the flow and the involved physical phenomena inside the combustion chamber of a HRE for the model presented in this paper

terms of total derivatives. For example, the continuity equation for an axisymmetric flow is written as Eq. (1):

$$\frac{\partial\rho}{\partial t}+\frac{\partial\rho u}{\partial x}+\frac{1}{r}\frac{\partial r\rho v}{\partial\eta}=0 \tag{1}$$

Because r is independent of the axial position, x, Eq. (1) can be rewritten as Eq. (2), which, through the radial integration and the application of the integral Leibnitz rule, results in Eq. (3). Here, a change in the coordinate reference system has been performed by defining the independent variable $\eta = R - r$, referenced to the solid fuel surface, in order to ease the manipulation and computation of the different equations.

$$\frac{\partial r\rho_e}{\partial t}+\frac{\partial r\rho_e u_e}{\partial x}+\frac{\partial r\rho_e v}{\partial\eta}=0 \tag{2}$$

$$\begin{aligned}
&\int_\delta^R \frac{\partial r\rho_e}{\partial t}d\eta+\int_\delta^R \frac{\partial r\rho_e u_e}{\partial x}d\eta+\int_\delta^R \frac{\partial r\rho_e v}{\partial\eta}d\eta=0\\
&\quad\rightarrow \frac{d}{dt}\int_\delta^R (R-\eta)\rho_e d\eta+(R-\delta)\rho_e\frac{d\delta}{dt}+\frac{d}{dx}\int_\delta^R (R-\eta)\rho_e u_e d\eta+(R-\delta)\rho_e u_e\frac{d\delta}{dx}+(R-\delta)\rho v|_\delta^R=0\\
&\qquad\rightarrow \frac{(R-\delta)^2}{2}\left(\frac{d\rho_e}{dt}+\frac{d\rho_e u_e}{dx}\right)+(R-\delta)\rho_e\left(\frac{dR}{dt}+u_e\frac{dR}{dx}\right)-(R-\delta)\rho_e v_\delta=0
\end{aligned} \tag{3}$$

A coupling between the equations of the core and the BL regions is established through the radial mass flux term $\rho_e v_\delta$ appearing in Eq. (3) and evaluated at the lower boundary of the core flow region (upper limit of the BL zone). The rest of the integral Euler equations: axial and radial momentum [Eqs. (4)(a) and (4)(b)], energy [Eq. (4)(c)] and mass fraction [Eqs. (4)(d) and (4)(e)], are obtained by proceeding in the same way than for the continuity equation previously presented. An order of magnitude analysis has been applied throughout all of them, allowing to neglect the axial derivatives face to the radial variations of a variable. To complete and close the system, an equation of state must be formulated. For simplicity, the ideal gas law is used [Eq. (5)].

$$\begin{cases} \rho_e \frac{du_e}{\partial t} + \rho_e u_e \frac{du_e}{\partial x} = -\frac{dP}{dx} & \text{(a)} \\ \frac{dP}{dr} = 0 & \text{(b)} \\ \rho_e \frac{dh_{t,e}}{dt} + \rho_e u_e \frac{dh_{t,e}}{dx} = \frac{dP}{dt} & \text{(c)} \\ \rho_e \frac{dY_{k,e}}{dt} + \rho_e u_e \frac{dY_{k,e}}{dx} = 0 \qquad \text{for } \ k = 1, 2 \ldots N_{sp} - 1 & \text{(d)} \\ \sum_{k=0}^{N_{sp}} Y_{k,e} = 1 & \text{(e)} \end{cases} \tag{4}$$

$$P_e = \rho_e \left(\sum_{k}^{N_{sp}} Y_{k,e} \frac{R_g}{\mathcal{M}_k} \right) T_e \tag{5}$$

2. Integral Boundary Layer Equations

The unsteady integral BL equations are obtained by integrating the Navier-Stokes equations of mass and momentum with respect to the radial coordinate over the boundary layer thickness, $0 \leq \eta \leq \delta$ [see Eqs. (6) and (7)]. The formulation of the equations is made in terms of the mean turbulent flow: the dependent variables are all interpreted as mean values, and no turbulent fluctuations are considered.

$$\int_0^{\delta} \frac{\partial r\rho}{\partial t} \,\mathrm{d}\eta + \int_0^{\delta} \frac{\partial r\rho u}{\partial x} \,\mathrm{d}\eta + (R - \eta)\rho v|_0^{\delta} = 0 \tag{6}$$

$$\int_0^{\delta} \frac{\partial (r\rho u)}{\partial t} \,\mathrm{d}\eta + \int_0^{\delta} \frac{\partial (r\rho u^2)}{\partial x} \,\mathrm{d}\eta + (R - \eta)\rho u v|_0^{\delta} = -\frac{dP}{dx} \int_0^{\delta} (R - \eta) \,\mathrm{d}\eta + (R - \eta)\tau|_0^{\delta} \tag{7}$$

The resulting equations involve the compressible integral quantities, δ^* and θ, corresponding to the displacement and momentum thicknesses, which, for an axisymmetric internal boundary layer, are given by Eq. (8) [26]. Another definition of these variables for axisymmetric flows, in function of the radial variable, may also be used in literature [26, 27]. However, they tend to overestimate δ^* and θ measurements for small diameter cylinders ($\delta/R \gg 1$). In order to extend the applicability of the model to a wide range of motor sizes, it has been considered wise to stay with the expressions given by Eq. (8), which also reduce to those of a flat plate boundary layer when $R \longrightarrow \infty$.

$$\begin{cases} R^2 - (R - \delta^*)^2 = \int_0^{\delta} \left(1 - \frac{\rho(\eta) u(\eta)}{\rho_e u_e}\right) 2r \, d\eta \\ (R - \delta^*)^2 - [R - (\theta + \delta^*)]^2 = \int_0^{\delta} \frac{\rho(\eta) u(\eta)}{\rho_e u_e} \left(1 - \frac{u(y)}{u_e}\right) 2r \, d\eta \end{cases} \tag{8}$$

The calculation of δ^* and θ in Eq. (8) requires the numerical computation of the integrals involved in this expression. Nevertheless, by reason of the high computational cost necessary to perform the integral numerically, the approximation

$\int_0^\delta \rho(\eta)u(\eta)\,d\eta \approx \bar{\rho}\int_0^\delta u(\eta)\,d\eta$ has been implemented. Here, $\bar{\rho}$ represents the averaged density over the BL in the axisymmetric flow configuration, calculated by using Eq. (5) applied to the averaged values of the involved variables over the BL, that is to say: $\bar{\rho} \approx \frac{P}{\bar{T}\sum_k^{N_{sp}} \bar{Y}_k \frac{R}{M_k}}$. In the latter, $\bar{T}$ and $\bar{Y}_k$ are computed by integrating their corresponding radial profiles (presented later in this section) over the axisymmetric BL. The calculation of the averaged value of any quantity, ϕ, over the BL is defined as $\bar{\phi} = \frac{1}{\int_0^\delta 2r\,d\eta}\int_0^\delta 2r\phi\,d\eta$. This simplification has allowed to greatly diminish the computational time. Nevertheless, when employing the proposed approximation in the HRE case, it has been observed a nearly constant difference of about 10 to 20% in the computed BL thickness and regression rate values with respect to the exact computation of the integral. This is associated to the shape of the temperature and density profiles over the BL and the strong gradients that are produced over this one when the flame is present, which makes the integral approximation by an averaged value slightly wrong. Several analysis have been performed to evaluate the discrepancies between the two calculation methods for a range of inlet pressures, temperatures, oxidizer mass fluxes, motor sizes and O/F couples. The differences found can be attenuated by applying constant corrector factors of 0.77 and 0.7 to the δ^*/δ and $(\delta^* + \theta)/\delta$ ratios, respectively, leading to a reduction of the discrepancies originally found in the BL thickness and regression rate values between both calculations of at least three times. The maximal errors associated to the application of these constant corrector factors between the different cases tested are about 6.75% (with a 95% trust interval).

Following the displacement and momentum thickness definitions, and proceeding like in Sec.II.A.1 to perform the integration of Eqs. (6) and (7), the integral equations of mass and axial quantity of momentum in the boundary layer result in Eqs. (9) and (10), respectively. The radial mass flux term at the BL edge ($\rho_e v_\delta$) appearing in the integral continuity equation of the core flow [Eq. (3)] has been introduced as the upper boundary condition when evaluating the integral of the radial mass flux over the BL thickness, coupling in this way, both core flow and boundary layer regions. In Eq. (9), $\rho_s v_s$ defines the gaseous mass flux at the wall produced by the pyrolysis of fuel.

$$\frac{\partial}{\partial t}\left\{\frac{1}{2}\left[R^2-(R-\delta)^2\right]\bar{\rho}\right\} + \frac{\partial}{\partial t}\left[\frac{1}{2}(R-\delta)^2\rho_e\right] + \frac{\partial}{\partial x}\left[\frac{1}{2}(R-\delta^*)^2\rho_e u_e\right] - \rho_s v_s R = 0 \tag{9}$$

$$\begin{aligned}\frac{1}{2}(R-\delta^*)^2 u_e\frac{\partial\rho_e}{\partial t} + \frac{1}{2}\left[(R-\delta^*)^2-(R-\delta)^2\right]\rho_e\frac{\partial u_e}{\partial t} + \rho_e u_e (R-\delta^*)\frac{\partial(R-\delta^*)}{\partial t} + \rho_e u_e^2\left[R-(\delta^*+\theta)\right]\frac{\partial\left[R-(\delta^*+\theta)\right]}{\partial x} \\ + \frac{1}{2}\left[R-(\delta^*+\theta)\right]^2 u_e^2\frac{\partial\rho_e}{\partial x} + \rho_e u_e\frac{\partial u_e}{\partial x}\left\{\left[R-(\delta^*+\theta)\right]^2 - \frac{1}{2}(R-\delta)^2\right\} = -\frac{\partial P}{\partial x}\frac{1}{2}\left[R^2-(R-\delta)^2\right] - \tau_{xy,s}R\end{aligned} \tag{10}$$

The viscous stress term at the wall appearing in Eq. (10) can be expressed in function of the skin friction coefficient: $\tau_{xy,s} = \frac{1}{2}\overline{\rho u^2}C_{f,x}$. Where the upper bar represents the averaged value of the corresponding variable in the BL region. C_f is a coefficient characterizing the friction along the wall. It is calculated by semiempirical expressions that depend generally on Re and the rugosity along the wall, and vary from one geometry to another. To model the entrance effects of the flow in the channel on the skin friction, the law provided by Zilliac and Karabeyoglu [28] in their modeling of the physics of a HRE [Eq. (11)] has been employed. In this expression, the Reynolds analogy has been used, which leads to an expression relating the Stanton number and the skin friction coefficient: $St = C_f/2$. Additionally, it has been seen that for the model developed in this paper, the set $C_1 = 1$, $\alpha = 0.125$ and $\beta = 0.5$, which results in a curve for $C_{f0}(x)/C_{f0,D}$ similar to the one proposed by Zilliac and Karabeyoglu, fits better with the local variation of the fuel port diameter found at the end of the burn for the experimental tests performed in the present research.

$$\frac{C_{f0}(x)}{C_{f0,D}} = 1 + C_1 Re_D^{-\alpha} \exp(-\beta x/D) \tag{11}$$

Concerning the friction coefficient in the developed region for the non-blowing case ($C_{f0,D}$) appearing in Eq. (11), the expression proposed by Bhatti and Shah [29] defined for the whole Re range for a flow in a circular duct without mass addition [Eq. (12)] has been used to estimate its value. Besides, the blowing effect produced by the fuel pyrolysis at the wall has an impact on the skin friction coefficient by diminishing its value with respect to the non-blowing case ($C_{f,0}$). Two empirical correlations are used in function of the blowing parameter, $B = \frac{\rho_f v_r}{\frac{1}{2} C_f \rho_e u_e}$ [see Eq. (13)].

$$C_{f0,D} = A + \frac{C}{Re^{1/m}} \tag{12}$$

$$\frac{C_f}{C_{f0}} = \begin{cases} B^{-0.68} & \text{for } 5 < B < 20 \\ \frac{1}{1+0.4B} & \text{for } B \leq 5 \end{cases} \quad \text{(Ref. [23])} \tag{13}$$

Moreover, the integration of the equations in the radial direction requires the knowledge of the radial distribution of the main variables over the BL. An empirical velocity profile reproducing the radial variation retrieved from experimental data is used as the closure relation. Under the modeling assumptions made in Sec.II, a turbulent velocity profile has been selected when integrating this variable over the BL thickness. Turbulent non-reactive flows in circular ducts have shown a power of the law velocity distribution given by Eq. (14) [30], with $n = 1/7$ for a hydrodynamically developing flow. In an actual HRE environment, a slight acceleration happens at the flame position, where gases are less dense. However, the deviation produced from the non-reactive velocity profile of Eq. (14) at this zone has been neglected in this model as it has been observed that it is not very significant [2]. This fact will allow to simplify the expression describing the velocity distribution and hence, the realization of the analytical integrals.

$$\frac{u}{u_e} = \left(\frac{\eta}{\delta}\right)^n \tag{14}$$

As regards to the combustion process taking place within the boundary layer, following the hypothesis presented in

Sec.II, the reactive zone is considered to be infinitely thin. The flame zone, situated at a certain distance from the fuel surface along the channel, corresponds to the zone of maximum temperature of the flow, and generates the thermal heat necessary to produce and sustain the degradation of the solid fuel. Its presence implies a change of sign in the temperature, density and mass fraction gradients over the BL thickness. To obtain the radial distribution of these variables, the flame position must be known. This is located where the stoichiometric conditions are met, hence, where both mass fractions of oxidizer and fuel are zero. The use of the Reynolds analogy [31] ($Le = 1$, $Pr = 1$) allows us to relate the mass and heat transfers, therefore establishing an equivalence between the velocity distribution in Eq. (14), the total enthalpy and the Shvab-Zeldovich scalar variable, $z = Y_F - Y_O/r_M$, profiles. Equation (15) presents the general form of this analogy. From this one, it is possible to retrieve the flame distance to the fuel surface by applying $z = 0$, which results in Eq. (16). The corresponding stoichiometric O/F ratio ($r_{M,st}$) is computed by considering solely CO_2 and H_2O products. A global one-step reaction of the form $n_{Ox}Ox + F \longrightarrow n_{CO2}CO_2 + n_{H2O}H_2O$ is used to determine, by a mole conservation analysis for each element that composes it (H, C, O, etc.), $r_{M,st} = (n_{Ox}\mathcal{M}_{Ox})/(\mathcal{M}_F)$, which allows the calculation of the adiabatic flame temperature (T_{fl}) through Gordon and McBride's tool for a given pressure and O/F couple. This simple combustion description by a single reaction mechanism has been already used in other HRE numerical models presented in literature [32–34].

$$\frac{u}{u_e} = \frac{h_t - h_{t,s}}{h_{t,e} - h_{t,s}} = \frac{z - z_s}{z_e - z_s} \tag{15}$$

$$\eta_{fl} = \delta \left(\frac{-z_s}{z_e - z_s} \right)^n \tag{16}$$

In order to represent the discontinuity present in the signs concerning the temperature and mass fractions radial distributions between the two regions adjacent to the flame zone in the BL, we introduce two different set of profiles for these variables that are a function of their relative position to the reactive zone, and whose shape is equivalent to the radial velocity profile (upon the Reynolds analogy principle) [see Eq. (17)]. The temperature profiles can be retrieved by defining the total enthalpy as $h_t = \sum_{k=1}^{N_{sp}} Y_k \left(\Delta H^o_{f,k} + \int_{T_{ref}}^{T} c_{p,k}\, \mathrm{d}T \right) + \frac{u^2+v^2}{2}$.

$$\begin{cases} \frac{h_t - h_{t,fl}}{h_{t,e} - h_{t,fl}} = \frac{Y_k - Y_{k,fl}}{Y_{k,e} - Y_{k,fl}} = \left(\frac{\eta - \eta_{fl}}{\delta - \eta_{fl}} \right)^n & \text{for } \eta_{fl} \leq \eta \leq \delta \\ \frac{h_t - h_{t,s}}{h_{t,fl} - h_{t,s}} = \frac{Y_k - Y_{k,s}}{Y_{k,fl} - Y_{k,s}} = \left(\frac{\eta}{\eta_{fl}} \right)^n & \text{for } 0 \leq \eta \leq \eta_{fl} \end{cases} \tag{17}$$

3. Boundary Conditions: Gas-Surface Interaction Model

The radial mass flux at the fuel surface ($\rho_s v_s$) appearing in Eq. (9) comes from the pyrolysis process happening in the combustion chamber. In order to close the system of equations resulting from the integration of the BL equations, it is required to know the boundary conditions at the fuel surface, which are formulated through the Gas-Surface Interaction model (GSI). This one has been used by several researchers [2–4, 35] to model fuel consumption inside a HRE combustion chamber by CFD codes and describe the physics in the vicinity of the wall. In this approach, mass and energy balances are applied at the solid / gaseous flow interface at each axial station x_i. Concerning the total mass balance, we consider that the mass lost during fuel degradation by pyrolysis is entirely transmitted to the flow by virtue of mass conservation [Eq. (18)]. As for the species mass balance [see Eq. (19)], pyrolysis species are transported to the flow by mass advection and diffusion from the surface. A representation of this latter balance for an infinitesimal control volume of legnth dx is shown in Fig.2a.

$$\underbrace{\rho_s v_s}_{\text{Mass flux of gases}} = \underbrace{\rho_f v_r}_{\text{Mass flux of fuel by ablation}} \tag{18}$$

$$\underbrace{\rho_{s+} v_{s+} Y_{k+}}_{\text{Mass flux of species } k \text{ by the gaseous flow}} - \underbrace{\rho_{s^+} D_{diff} \frac{\partial Y_k}{\partial \eta}\bigg|_{s^+}}_{\text{Diffusion mass flux of species } k} = \underbrace{\dot{\omega}_k(T_s)}_{\text{Production mass flux of species } k \text{ by reaction with the fuel surface}} \tag{19}$$

The gradient of mass fraction evaluated at the fuel surface using the profile defined through Eq. (17) being null for a turbulent flow, the diffusion term is expressed by a mass film coefficient [Eq. (20)]. Additionally, through the Reynolds analogy, we have $\frac{h_D}{h_{conv}} = \frac{D_{diff}}{k}\left(\frac{Sc}{Pr}\right)^{1/3} \approx \frac{1}{\rho c_p}$ and $St = \frac{Nu}{RePr} \approx \frac{C_f}{2}$. Since $Nu = \frac{h_{conv} D}{k}$, the heat and mass transfer coefficients can be determined from the skin friction coefficient (C_f) correlations.

$$-\rho_{s^+} D_{diff} \frac{\partial Y_k}{\partial \eta}\bigg|_{s^+} = \rho_{s^+} h_D \left(Y_{k,s} - Y_{k,fl}\right) \tag{20}$$

Moreover, because pyrolysis is the only reaction happenning at the surface and as this is considered to be monospecies, the source term of Eq. (19), $\dot{\omega}_i$, is null except for the fuel species. By continuity of mass, the sum of all source terms in Eq. (19) must equal the total mass flux: $\sum_{k=1}^{N_{sp}} \dot{\omega}_k = \sum_{k=1}^{N_{pyr}} \dot{\omega}_{pyr,k} = \sum_{k=1}^{N_{pyr}} \frac{\nu_{pyr,k} \mathcal{M}_{pyr_k} G_f}{\mathcal{M}_f}$.

Finally, an energy balance is performed. Through its surface, the fuel receives the convective heat flux by the presence of the thermal boundary layer and the radiative heat flux from the flame zone. Besides, enthalpies of species resulting from fuel pyrolysis are transported to the flow by advection and mass diffusion. Part of the heat flux received at the surface that is not used for pyrolysis is transmitted into the fuel by conduction. Because of fuel degradation, a certain amount of the enthalpy of the solid is transmitted to the flow. Equation (21) presents the balance of the energy exchanges at the fuel surface. In the formulation, the diffusive transfers have not been considered because they are negligible in comparison with the convective heat contribution. Moreover, as it was mentioned in Sec. II, radiative transfers are not taken into account in this first modeling approach. The energy balance at the fuel surface for an infinitesimal control volume of length dx is illustrated in Fig. 2b.

$$\underbrace{\sum_{k=1}^{N_{sp}} \dot{\omega}_i [\Delta H^0_{f,k} + \int_{T_{ref}}^{T_w} c_{p,k}(T)\, dT]}_{\text{Chemical flux from pyrolysis}} - \underbrace{k_g \frac{\partial T}{\partial \eta}\bigg|_{s+}}_{\text{Convective flux}} \quad = \quad - \underbrace{k_f \frac{\partial T}{\partial \eta}\bigg|_{s-}}_{\text{Heat flux in fuel}} + \underbrace{\rho_f v_r (\Delta H^0_{f,s} + c_{p,s}(T_s - T_{ref})}_{\text{Enthalpy transport from fuel by regression}} \tag{21}$$

As it was performed with the diffusion mass transport term in the species mass balance at the fuel surface [Eq. (19)], the gas convection term in Eq. (21) is expressed in function of a thermal coefficient, h_{conv}, in the Newton convection law form [see Eq. (22)]. Furthermore, the enthalpy of pyrolysis or thermal heat of degradation, ΔH_{pyr}, appearing in the energy equation at the fuel surface [Eq. (21)], is a known quantity, following the expression given by Eq. (23).

$$k_g \frac{\partial T}{\partial \eta}\bigg|_{s^+} = h_{conv} \left(T_{fl} - T_s\right) \tag{22}$$

$$\Delta H_{pyr} = \sum_{k=1}^{N_{pyr}} \frac{\dot{\omega}}{\rho_f v_r} \left(\Delta H^0_{f,k} + \int_{T_{ref}}^{T_s} c_{p,k}\, dT\right) - \left[\Delta H^0_{f,s} + c_{p,s}(T_s - T_{ref})\right] \tag{23}$$

The solid fuel moving at a rate v_r can be considered as a semi-infinite solid that is characterized by the transient heat equation [Eq. (24)] with the boundary conditions: $T(\eta = 0, t) = T_s$; $T(\eta \rightarrow -\infty, t) = T_{ref} = T(\eta, t = 0)$. This equation is solved through a Laplace transformation, resulting in Eq. (25) that represents the solid conductive heat flux.

$$\frac{\partial^2 T}{\partial \eta^2}(\eta, t) - \frac{v_r}{a_{thermal}} \frac{\partial T}{\partial \eta}(\eta, t) = \frac{1}{a_{thermal}} \frac{\partial T}{\partial t}(\eta, t) \tag{24}$$

$$k_f \frac{\partial T}{\partial \eta}\bigg|_{s^-} = \frac{\rho_f v_r c_{p,fuel} \left(T_s - T_{ref}\right)}{2} \left[1 + erf\left(\frac{v_r}{2} \sqrt{\frac{t}{a_{thermal}}}\right)\right] + k_f \frac{\left(T_s - T_{ref}\right)}{\sqrt{\pi a_{thermal} t}} e^{-\frac{v_r^2 t}{4 a_{thermal}}} \tag{25}$$

Eventually, the fuel regression rate is described by an Arrhenius law relating the fuel ablation with the surface temperature [Eq. (26)]. Values of both coefficients (A_d, E_a) in Eq. (26) as well as the thermophysical properties of the solid fuel can vary widly from one reference to another [36–38]. Further sensitivity studies need to be performed in the future to determine the impact of some of these parameters on the results provided by the code. Table 1 presents the thermophysical characteristics specified in the code for both HTPB and HDPE fuels.

$$v_r = A_d \exp\left(-\frac{E_a}{R T_s}\right) \tag{26}$$

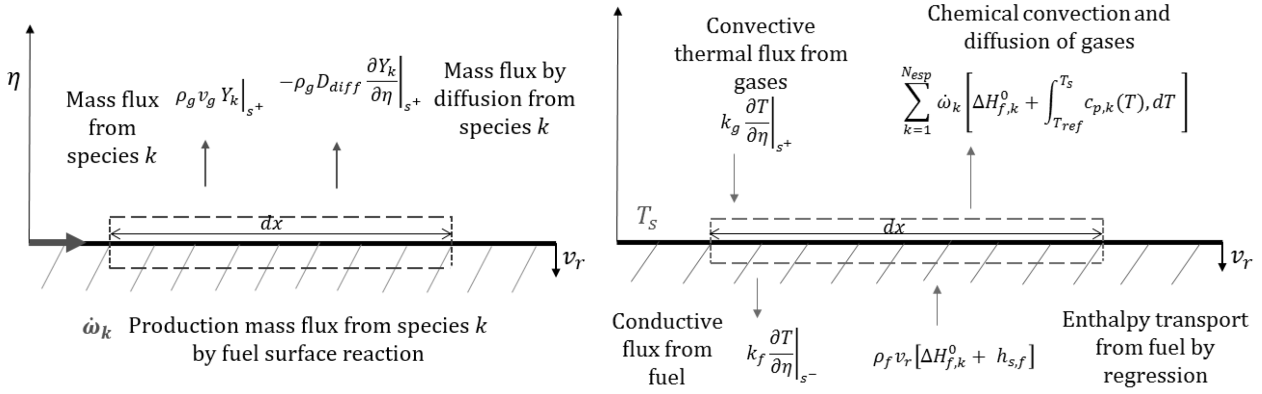

(a) Species mass balance at the fuel surface. **(b) Energy balance at the fuel surface.**

Fig. 2 Gas-Surface Interaction model at the fuel wall.

Table 1 Thermophysical properties of the HTPB [36, 37] and HDPE [38] solid fuels.

Variable	HTPB	HDPE
A_d	3.965 ($T_s \leq 722$ K)	4780
	0.01104 ($T_s > 722$ K)	
E_a	13.35×10^3 cal/mol ($T_s \leq 722$ K)	125.604×10^3
	4.91×10^3 cal/mol ($T_s > 722$ K)	
ρ_f	920	960
$c_{p,f}$	1632	1850
k_f	0.1506	0.4
ΔH_{pyr}	1.8×10^6	2.72×10^6
T_{vap}	420	415

B. Numerical Method Resolution

A Finite Difference Method (FDM) is used to discretize the numerical domain. Other authors [16, 32, 39] in the HRE modeling field have already employed this method to solve numerically the physical problem in the combustion chamber. In our model, the chamber is divided in N points or nodes along the axial direction (x_i, with $i = 1, 2..., N$), separated by a finite and constant distance (Δx). Each one of them is defined by the set of differential equations (continuity, quantity of momentum, energy, etc.) that has been presented in Sec II.A. These equations are evaluated and solved at each axial position, which allows the computation of the corresponding dependant variables at every node, and hence, the determination of the axial distribution of these along the chamber.

The set of Ordinary Differential Equations (ODEs) is solved by a two-level implicit method for time derivatives: the backward Euler first-order scheme, which evaluates the source terms at the currrent time step. Hence, $\phi^{n+1} = \phi^n + f\left(t_{n+1}, \phi^{n+1}\right)\Delta t$. This is an unconditionnally stable scheme, where errors appearing during the solution finding process are not magnified, as they are enclosed within a concrete range. That consequently makes it possible to take longer time steps without risk of appearence of instabilities and thus, to reduce the number of iterations. As regards to the spatial scheme to compute the axial derivatives, a first-order backward difference scheme that uses the information from the previous spatial points of the grid is chosen. Spatial derivatives are then calculated as $\frac{\partial \phi}{\partial x} = \frac{\phi_i - \phi_{i-1}}{x_i - x_{i-1}}$. For example, the discretized form of the equation of axial quantity of momentum in the core flow [Eq. (4)(a)], at a node i, results in Eq. (27).

$$\rho^n_{e,i} \frac{u^n_{e,i} - u^{n-1}_{e,i}}{\Delta t} + \rho^n_{e,i} u^n_{e,i} \frac{u^n_{e,i} - u^n_{e,i-1}}{x_i - x_{i-1}} = -\frac{P^n_{e,i} - P^n_{e,i-1}}{x_i - x_{i-1}} \tag{27}$$

A globally convergent Newton-Raphson method (NR) is employed to solve the system of the discretized equations for each node with a specified residual of 10^{-8}. This ensures that the discretized equations representing the conservation of mass and the thermodynamic quantities between the current node and the previous one are greatly satisfied. This quasi-Newton method of global convergence is a robust technique that combines the quadratic convergence of the classical NR method for the zero-root finding technique of a system of equations with the backtracking line search strategy: an algorithm allowing to determine the maximum quantity of steps to advance in a given direction that succeeds in a sufficiently satisfactory reduction of the objective function, thus guaranteeing progress at each iteration towards the final solution. In addition, a verification of the conservation of the mass, quantity of momentum, energy and mass fraction variables inside the combustion chamber control volume was performed with the purpose of validating the computing capacity of the code. All these quantites proven to be conserved, providing maximum residuals of 10^{-4}.

Concerning the numerical ressources demanded by the computational resolution of the model developed in this article, it has been observed that the computational time is very dependent on the spatial and time discretizations (Δx and Δt, respectively). Indeed, the computing CPU time of the implemented numerical algorithm follows a power law of the form $\Delta t^{-0.95}$ with the selected time step. As for the spatial discretization, the computing time increases with $\Delta x^{0.61}$. In general, using the presented pseudo 2-D model for the simulation of a combustion chamber (constituted by an optimized number of 100 nodes) and a 1-D model to calculate the flow inside the nozzle, a solution at a specific instant of the test can be obtained in around 5 seconds of CPU time on a desktop computer. With an appropiate time step of 0.1 s, a HRE firing during 5 seconds can be simulated in 5 minutes of CPU time on a desktop computer. On the contrary, a 2-D axisymmetrical single instant RANS simulation of a HRE combustion chamber, performed with a CFD tool such as CEDRE [40], can take more than 2 hours CPU on our supercomputer (SATOR) [41].

III. Numerical Results

Several studies have been performed with the intention of assessing the validity of the presented model and its capability to capture the most important effects of the physics happening inside the combustion chamber of a HRE. Firstly, a verification analysis to prove the capacity of an integral method to well reproduce the boundary layer development is performed in a non-reactive flow case. Concerning the HRE case (reactive flow in the channel), the influence of the oxidizer mass flux applied to three different O/F couples as well as the impact of motor size on fuel consumption are evaluated for a simulation in the steady-state regime. Eventually, a comparison with three specific tests performed at our laboratory has been tackled to evaluate the numerical results of the present model with time.

A. Verifications for a Non-reactive flow

Before assessing the flow inside the combustion chamber of a HRE, several preliminary analysis have been performed in a steady, non-reactive flow.

A first verification effort has been made to reproduce the boundary layer over a flat plate in the laminar and turbulent regimes by using the Cartesian coordinates version of the equations presented in Secs. II.A.1 and II.A.2 because of their easier formulation over the axisymmetric one. In our model, the BL thickness and the flame position have a significant impact on the heat transfers to the wall and thus on the fuel consumption rate. Therefore, the former variable, together with the displacement and momentum thicknesses have been used to assess our model in simple (non-reactive) flow cases. On account of the existance of an exact solution for a laminar BL ($Re_x < 5 \times 10^5$) over a flat plate, a verification in this regime has been performed. The only difference with respect to the turbulent regime resides in the use of a different empirical velocity profile, describing, in this case, the radial velocity distribution inside a laminar BL as: $\frac{u}{u_e} = \frac{3}{2}\left(\frac{\eta}{\delta}\right) - \frac{1}{2}\left(\frac{\eta}{\delta}\right)^3$ [42]. Hence, the exact Blasius solution [43] (flow over an adiabatic flat plate with a zero pressure gradient) has been compared to the solution provided by the integral method previously presented. Our integral method, has produced relative differences lower than 6% in comparison with the self-similar Blasius solution for the several boundary layer characteristic thicknesses (δ, δ^* and θ), which is thought to be a good estimation when taking into account the simplifications carried out in the integral model. With respect to the turbulent flow case -flow regime found in a HRE combustion chamber-, the solution provided by the code for a $Re_L = 5 \times 10^6$ along a wall of one meter length has been first compared to the integral method solution given by Prandtl [44], based on the resolution of the Von Karman's momentum equation (with a zero pressure gradient). Here, Prandtl used the radial velocity distribution defined in Eq. (14). The relative differences between both boundary layer solutions, under 1.5%, are explained by the numerical errors occuring during computation and the account for a weak pressure gradient in our simulation. Additionally, a comparison with a more precise / sophisticated model that solves the 2-D set of differential equations for the mean flow in the BL was performed. The author [42] employed an eddy-viscosity model to describe the turbulent flow (Reynolds stress) across the layer. This gave relative discrepancies with our integral apporach inferior to 9.5% and 15% for the displacement and momentum thicknesses, respectively. The good agreement between our computation and Prandtl's analytical solution let us validate the numerical resolution capacity of our code. Moreover, the comparison with the 2-D numerical resolution is considered to be good enough too when taking into account the simplicity of our model for its application to the engine predesign phases.

The next verification step for a non-reactive flow case has been focused on the effect of surface blowing on a flat plate. The analytical solution of the von Karman's integral equation for a zero pressure gradient over a porous wall with mass injection is presented in Eq. (28), where the relation of C_f with the blowing parameter given in Eq. (13) for a low mass flow injection has been considered. In this case, the skin friction coefficient without blowing appearing in Eq. (13) corresponds to that of a flat plate, which is defined by $C_{f0} = 0.059Re_x^{-0.2}$ [42]. The conditions of Simpson's 1228667 experiment [45] over a plate suffering an averaged mass flux injection normal to the wall of $G_w = (\rho v)_w = 0.99 \times 10^{-3}\rho_e u_e$ on a turbulent BL have been reproduced. Figure 3a illustrates a comparison between both the analytical and our computed displacement thickness with the experimental measurements from Simpson. The corresponding numerical solution by Schetz and Favin [46] of the 2-D differential equations of the mean turbulent flow using an extended Reichardt eddy viscosity model for the BL description is depicted as well.

$$\theta(x) = \frac{0.0295}{0.8}\left(\frac{\mu}{G_e}\right)^{0.2} x^{0.8} + 0.6\frac{G_w}{G_e}x \tag{28}$$

Relative differences between our solution and the analytical one are about 2% for the several characteristic thicknesses of the BL. These discrepancies may be linked to the absence of a pressure gradient in the analytical case, resulting in a thicker BL with respect to our computation. In relation to the experimental results, the biggest relative discrepancies are found at the beginning of the plate, where they may reach 40% for the displacement thickness and 34% for the momentum thickness, descending to 15% and 4% downstream, respectively. As for the numerical 2-D computation of Schetz and Favin, the axial evolution of δ^* and θ fits better the experimental reference at the start of the BL growth, resulting in a much lesser agreement with the Simpson et al.'s work downstream. An increase in the BL thickness associated to mass injection at the wall is found by our numerical results (see Fig. 3b), which is in agreement with the analytical solution and the literature data [11].

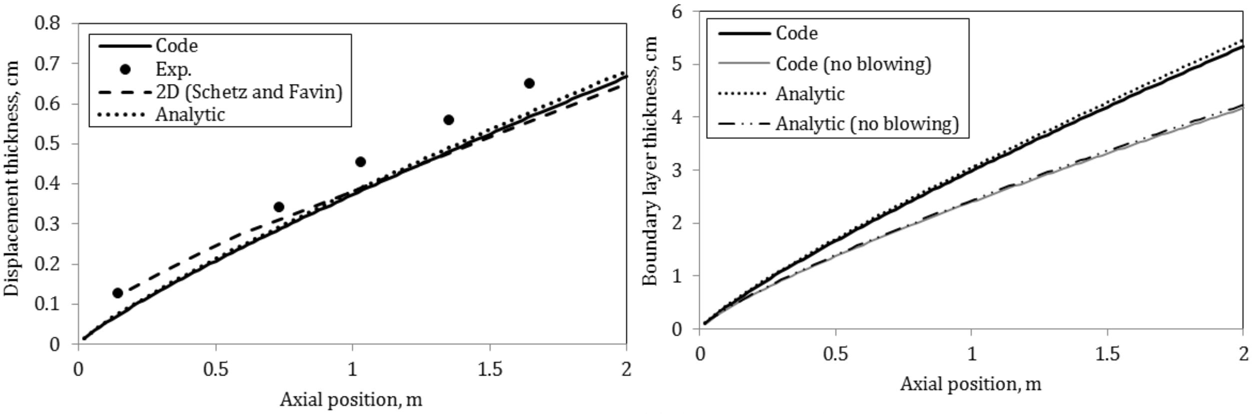

(a) Comparison of the computed displacement thickness with the references [45, 46] for a flat plate with mass injection.

(b) Comparison of the analytical and numerical boundary layer thickness over a flat plate with and without mass injection.

Fig. 3 Effect of blowing on a turbulent boundary layer development over an adiabatic flat plate.

Moreover, the ability of our model to simulate a compressible flow has been assessed. Whitfield [47] presented also an integral BL formulation for a compressible, turbulent boundary layer over a non-permeable, adiabatic wall. The dissimilarities between Whitfield's model and ours reside in the expressions employed for the description of C_f, the velocity-temperature relation, the introduction of several shape factor (δ^*/θ) correlations modified for a compressible flow, and the different analytical expression used for the radial velocity description over the BL thickness. Boundary layer displacement and momentum thickness experimental measurements by Pasiuk et al. [48] of a compressible and turbulent flow over an adiabatic flat plate have been compared to our calculations and Whitfield's. The flow was subject to a favorable pressure gradient, with a Mach number varying from 1.5 to 3 along the BL edge. Figure 4a depicts the momentum thickness evolution along the wall for the three methods, showing a good agreement between our integral model and Witfield's, but also with the experiment of Pasiuk et al..

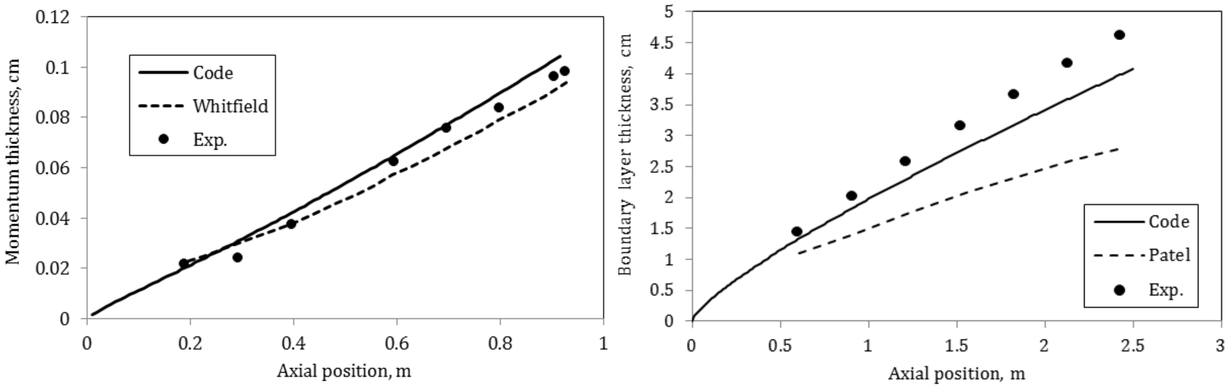

(a) Comparison of the computed momentum thickness with the references [47, 48] for a compressible flow over an adiabatic flat plate with a favourable pressure gradient.

(b) Comparison of the computed boundary layer thickness with the references [27, 49] over a cylinder of constant radius.

Fig. 4 Effect of blowing on the boundary layer development over an adiabatic flat plate.

To finish with the simple verification tests and validate the axisymmetric formulation of the model presented in Sec. II.A.2 for the non-reactive flow case, a prediction of the development of an axisymmetric turbulent BL has been performed along the axis of a constant radius cylinder. A formulation for thick, axisymmetric boundary layers using an integral approach has been already tackled by Patel [27]. The numerical results obtained by the model presented in this article have been thus compared to Patel's numerical solution as well as to one set of experimental data of Yu [49] over a cylinder of 2.5 cm radius and with a radius-based Reynolds of 15250. Figure 4b represents the boundary layer growth over the cylinder for the three methods. The existing discrepancies between his computation and the experiment, more significant for the BL and momentum thicknesses, may be explained in part by the presence of a non-zero pressure gradient in the experiment, as well as to the employed velocity profile and shape factor expressions in their calculations. In comparison with our results, when using the expressions for the displacement and momentum thicknesses given by Eq. (8), we get to improve Patel's results for the boundary layer thickness with respect to the experimental data (reducing them from 40 to 13%), but on the contrary, our momentum thickness is much more underestimated (passing from 20%

error for Patel's, to 33% in our case). Because it has been observed that the BL thickness is the parameter having a significant impact on the heat transfers to the fuel surface, and our estimation of this one is considered to be sufficiently good (differences remaining lower than 13%) compared with the experimental result, this verification step is considered as achieved despite the greater differences found in the momentum thickness values.

In conclusion, comparisons between our model and the experimental data or known analytical solutions regarding the description of the boundary layer have provided sufficiently satisfactory results and hence, allowed to validate the model for simple flow cases, in the non-reactive and stationary regime.

B. Verifications for a Reactive flow case: Influence of mass flux on the fuel Regression rate for Different Compounds

In order to assess the solution provided by the model concerning the reactive flow inside a HRE, and hence, validate the combustion model implemented in the code through Gordon and McBride's tool and the GSI model, several analysis evaluating and comparing the fuel consumption rate in different motor conditions with some reference data present in literature have been performed, since this variable is a key parameter in the HRE performances calculation. Sources have shown that the mass flux flowing through the combustion chamber affect significantly the fuel consumption. Hence, in the present subsection, an analysis of the influence of this parameter on the computed fuel regression rate values has been performed in order to check the good agreement to the references. In this context, Marxman and Gilbert [50] provided an expression directly relating the fuel regression rate to the specific mass flow rate crossing the channel [see Eq. (29)], where only the convection contribution to the thermal flux (with no radiation) was considered.

$$v_r = aG_{tot}^n \approx aG_{ox}^n = a\left(\frac{\dot{m}_{ox}}{\pi r^2}\right)^n \tag{29}$$

In Eq. (29) a and n are constant preexponential and exponential coefficients, respectively. Both of them result from a polynomial adjustment coming from empirical data, generally leading to a coefficient of determination, R^2, that can vary in a wide range (approximately from 0.43 to 0.99 [10, 51–53]). This *power law* is most employed in numerical models to describe HRE fuel pyrolysis in a simple and direct way. However, the use of this kind of law in a combustion chamber model would require the knowledge of the a and n coefficients and thus, would demand to perform or have already performed the test campaign at the specific conditions that would be simulated numerically in order to continue to obtain a good estimation (errors inferior to 5%) of the regression rate values for a given mass flux range. In case of employing laws already existing in literature, the resulting errors might not be negligible in some cases, since these coefficients may vary greatly (as it will be shown after) depending on the experimental conditions of the tests used to generate it; the geometric shape and size of the fuel solid block, as well as the thermomechanical properties that characterize it, which are influenced by its manufacturing process; the type of injection of the oxidizer; and the O/F pair among others. This hinders the general applicability of these laws to describe fuel pyrolysis for an engine predesign code like the one envisaged in this article. On the contrary, an Arrhenius law [see Eq. (26)] depends only on the properties of the fuel and on the surface temperature (related to the physiscs inside the chamber), which will allow the simulation of a more extensive variety of HRE configurations and conditions.

A comparison of the computed space-averaged fuel regression rate values with those from literature has been developed hereafter for several oxidizer mass fluxes and O/F couples. The reference values used for this comparison come from empirical laws of the form of Eq. (29) established by their authors through the realization of experimental test campaigns. Hence, comparisons have been made for the O_2 / HTPB couple (Fig. 5) with Refs. [51, 54–60]; the N_2O / High Density Polyethylene (HDPE) (Fig. 6a) with Refs. [52, 61, 62]; and 90% H_2O_2 / HTPB (Fig. 6b) with Refs. [63, 64]. In the latter, a catalyst injection that produces the decomposition of hydrogen peroxide into gaseous oxygen and water vapor has been used. In all of the references, lab-scale motors were employed. The dimensions of the simulated engine in the present code corresponded also to a lab-scale motor of D = 25 mm and L = 240 mm (dimensions of the hybrid engine from our laboratory). The range of analysis for the mass fluxes went from 25 kg/m^2/s to 400 kg/m^2/s, which corresponded to the limits studied by some of the references when characterizing Eq. (29) to match with experimental data. The evaluation of the numerical results for higher oxidizer mass fluxes has not been pursued for this analysis since these semiempirical laws were not constructed by using data corresponding to a larger mass flux range. Moreover, because of the gas-phase chemical reactions effect, the growth tendency of the regression rate with the mass flux changes from the one established by the law when overpassed a certain value of specific mass flow [65]. Experimental tests at higher mass fluxes will be performed in our laboratory in the future to establish the limits of our model in relation to this parameter.

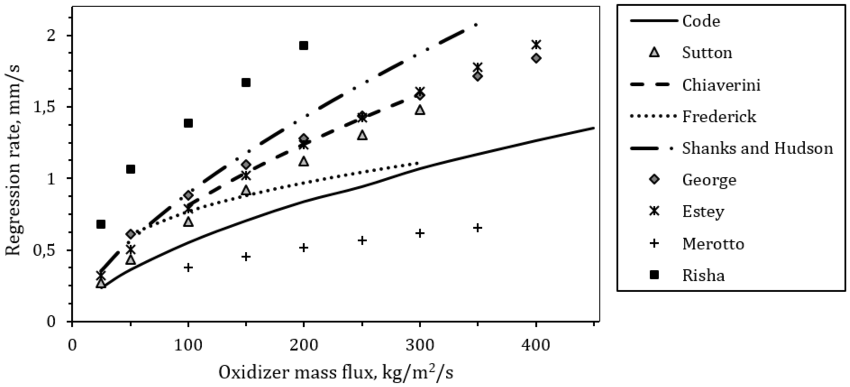

Fig. 5 Computed fuel regression rate in function of the oxidizer mass flux for the O_2 / HTPB couple and comparison with the literature data [51, 54–60].

Provided numerical regression rate results are found to lay on the lower region defined by the literature values in the analyzed mass flux range for the three couples studied. Empirical laws from the references present differences in the *a* and *n* values that can be quite significant for some O/F couples. These inconsistencies are found to be larger for the O_2 / HTPB couple specially, where the relative differences found between the numerical and the literature burn rates values are also more important when compared with the other two studied couples. Therefore, the current analysis should be mainly considered as a verification study as regards to the order of magnitude of v_r. A full comparison with dedicated experimental tests remains essential to validate the developed combustion chamber model for a HRE. For the O_2 / HTPB couple, the relative differences tend to increase with the introduced mass flux, and they can attain values up to 51% when comparing with the laws supplying a higher estimation of the ablation rate than ours. On the opposite, for both couples N_2O / HDPE and 90% H_2O_2 / HTPB, the relative differences decrease while increasing G_{ox}, and they present a better agreement with the literature laws for higher specific mass flows. In this article, the percentage error (ε) of any numerical quantity (ϕ_{num}) with respect to the corresponding experimental value (ϕ_{exp}) has been calculated following the expression $\varepsilon = \frac{|\phi_{exp} - \phi_{num}|}{\phi_{exp}} \times 100$.

This study has permitted to validate the influence of burn rate upon the oxidizer mass flux, showing an increase in fuel consumption with this variable. Possible error sources at the origin of the discrepancies are detailed hereafter.

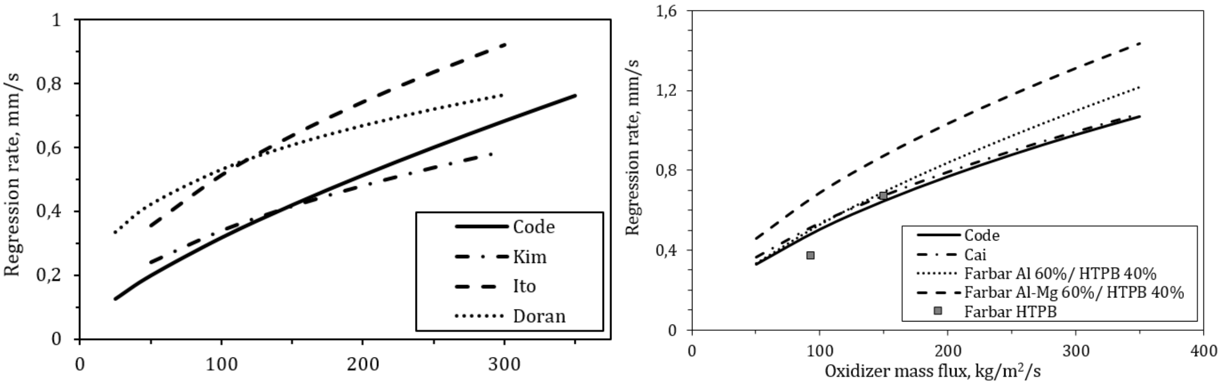

(a) N_2O **/ HDPE couple. Comparison with Refs. [52, 61, 62].**

(b) 90% H_2O_2 **/ HTPB couple. Comparison with Refs. [63, 64].**

Fig. 6 Computed fuel regression rate in function of the oxidizer mass flux and comparison with literature data.

1. Error Sources

The existing differences observed between the numerical results obtained by the presented code and the literature data using a semiempirical expression in the form of Eq. (29) can come from a diverse kind of sources, some of them may result from the simplifications taken during the modeling of the physics phenomena of the combustion chamber.

First of all, laws such as Eq. (29) do not consider the impact of motor size. Estey et al. [58] observed bigger errors in the estimation of the regression rate through their Eq. (29) law when applied to larger motors. It is not known with certainty the range of fuel port diameters in which these laws can be applied to obtain results with a good correlation with the experiments. In turn, attention must be taken when comparing with laws retrieved from slab-burner setups, such as the one from Refs. [51, 59], since this fuel block geometry do not correspond with the axisymmetric flow formulation used for the obtention of the numerical results.

Besides that, it has been observed that the addition of metallic particles to the fuel (such as Al or MgH_2) or additives like carbon black or catalyst particules as performed in the references [56, 58, 63] produces an enhancement of the pyrolysis process that could generate an increase in the fuel regression rate from 26% to 300% [55, 57], improvement that is also more important for higher mass flux conditions. Nevertheless, the simulations in this paper have involved solely the reaction between the oxydizer and the predominant pyrolysis product, not taking into consideration the participation of other metallic components.

As a matter of fact, our model may present some sensitive points too. The first may reside in the BL modeling. This is related to several factors, such as the deviation of the radial profiles of the variables in the BL from the real ones, the employed skin friction coefficient law, the numerical approximations taken in the equations, etc. Another sensitive aspect is related to the combustion process (modeled as infinitely fast and with an approximate chemical kinetics) and, specially, to the thermal gas convection and species diffusion modeling in the GSI exchange transfers. Additionally, radiative heat transfers may have a significant impact on fuel consumption, specially at low mass fluxes or fuel rich mixtures, when soot production will be important and can account up to 80% of the total radiative flux [51]. In this case, radiation acquire a major importance over turbulent convection and could produce an increase in the obtained fuel regression rate from 5 to 35% [3, 50, 66]. Empirical expressions quantifying soot radiation could be employed in the model, but at this moment they only exist for the O_2 / HTPB couple [67], whose fuel is known to produce a great deal of soot particles. Finally, the last factor related to the modeling that could have a non-negligible impact on the results is the specified thermophysical properties of the solid propellant, such as density, specific heat, depolymerization enthalpy of the fuel or even the coefficients used in the Arrhenius law. It has been noticed that decreasing the fuel density or the specific heat of the fuel can increase up to 6% the value of v_r computed by the code when a variation of the same order is performed in these quantities. An extensive sensitivity analysis will be performed in the future once the validation process of the model has been completed and hence, the possible necessary changes to improve the model precision have been already applied.

Furthermore, as it was observed by Refs. [32, 53, 68, 69], the chamber pressure has been found to have an influence on the regression rate, producing at most, a 5% of burn rate variations in our model. This effect has already been considered in several studies [52, 55, 58] through empirical laws akin to Eq. (29).

Moreover, from literature data, the local fuel consumption is found to be very dependent on the entrance characteristics to the fuel channel, which influence then, the aerodynamics in the combustion chamber and hence, the thermal exchanges with the fuel. These characteristics are defined by the injection type [53, 70, 71] and the precombustion chamber features such as its dimensions [10]. The formulation presented in this paper has been developed for an axial injection type. Indeed, compared to radial injection, Carmicino and Sorge [72] observed higher and less uniform regression rate values for an axial injection. This was due to oxidizer jet dynamics at the impinging zone, where fuel consumption attains a maximum, especially when mass flux is lower. Also, Knuth et al. [70] found that a swirl injection can produce up to seven times the regression rate when compared with an axial injection type. In fact, only a fraction of the references used for the comparison with the solution of the presented model specified the type of injection employed in their tests, being uncertain whether any of them used an axial injection or another.

Eventually, the last element that can be behind the differences found between the reference results and our numerical model is the technique used to determine the experimental space-averaged diameter of the fuel block at the end of the test. This value is required for the estimation of the experimental averaged ablation rate, $v_r = \frac{\bar{D}_{end} - D_0}{2t_{hyb}}$, which is used in the correlations to generate the semiempirical laws [see Eq. (29)]. The computation of this diameter can be done by two techniques: geometrically, through the measurement of the averaged remaining fuel thickness of the block [51]; or by performing a fuel mass conservation in the chamber at the end of the test [52, 55, 57, 59, 62–64]. Regression rate may vary up to a 15% using one method or the other due to the regression of the lateral faces of the solid fuel.

C. Verifications for a Reactive flow case: Scale-up Effects

Several researchers have already reported the influence of motor size on the experimental regression rate [57, 64]. For the same mass flux, when increasing the port diameter, the flame moves furher away from the fuel surface, therefore reducing the temperature gradient and the convective heat transfer to the wall. Moreover, for larger motors, the BL occupies in proportion a smaller part of the channel, and the flame remains confined closer to the wall. This fact may leave a portion of the core unburned, consequently decreasing the combustion efficiency compared with subscale motors. A numerical test has been performed to analyze the influence of motor size along with the oxidizer mass flux for three different port fuel diameters: 25, 50 and 100 mm. The same simulation conditions at the inlet of the chamber than the ones employed by Cai et al. [64] in their article have been used: $T_{in} = 1000$ K and $P_{in} = 2.4$ MPa for a 90% H_2O_2 / HTPB couple. For all the configurations, the non-dimensional chamber length was held constant at $L/D = 23.2$.

Figure 7a illustrates the dependence of the computed regression rate results with the specific mass flow rate for the three different diameters, and compares them with the CFD results of Cai et al. A good general agreement between both is found, whereas the biggest absolute errors are of about 20%. Despite the fact that the slopes of the logarithmic curves obtained by both codes are not exactly the same, the current model still shows the correct qualitative influence of the motor size on the ablation rate, thus describing a decrease in fuel consumption when increasing the fuel port diameter. Moreover, in agreement with Cai et al. theoretical analysis, we find that fuel consumption rate depends on the fuel port diameter to the power of -0.2, as it is shown by the overlapping of curves for the three diamaters in Fig. 7b, where the equivalent regression rate ($v_r d^{0.2}$) is displayed in function of the oxidizer mass flux.

D. Validation of the Pseudo 2-D Model by Comparison with the Experimental Tests of our Laboratory

To continue with the validation of the code developed in this research, a complete numerical simulation reproducing a full test in a HRE must be evaluated during the operational time of the engine, so that the temporal evolution of the

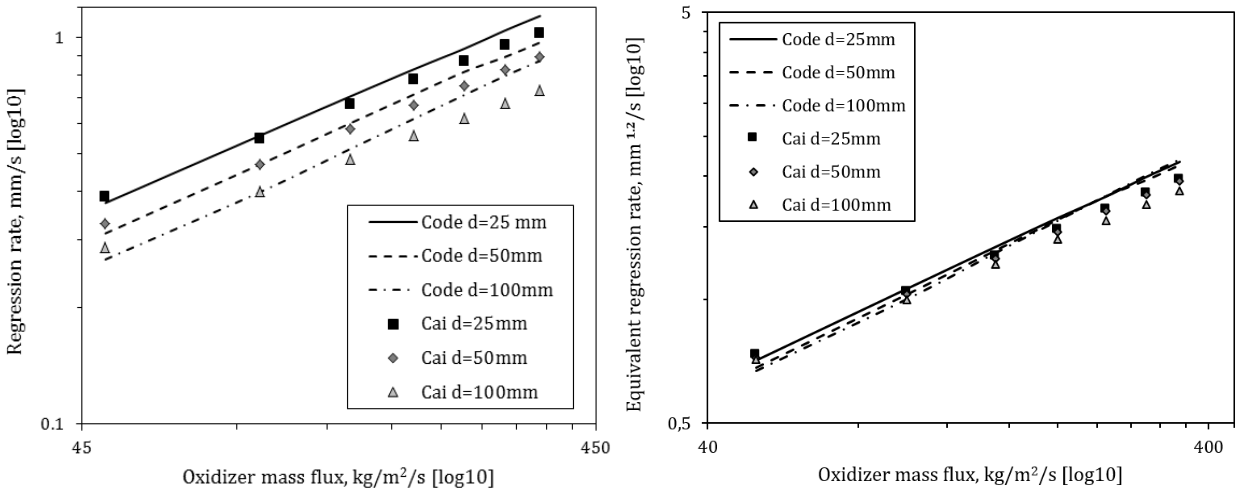

(a) Evolution of the fuel regression rate with the oxidizer mass flux for combustion chambers of different sizes.

(b) Evolution of the equivalent fuel regression rate with the oxidizer mass flux for combustion chambers of different sizes.

Fig. 7 Scale-up effects on fuel consumption rate. Comparison with Cai et al. [64] numerical solution.

main variables can be assessed. To proceed, a comparison has been made between the numerical results obtained by the pseudo 2-D code with three different experimental tests conducted in HYCAT, the HRE of our laboratory: HYCAT 12, 23 and 26. All of them employed 87.5% H_2O_2 with HDPE as the O/F couple. A brief description of the HYCAT motor, the measurement techniques, as well as the operational conditions and the outcome of the aformentioned tests can be found in Ref. [73].

Thanks to the catalytic injection system integrated in the motor, no pyrotechnic device is required to ignite the engine and initiate the combustion process. In a characteristic HYCAT test, two stages are distinguished: the monopropellant (*non-reactive*) phase with the oxidizer as the only species in the flow, in which no combustion has taken place yet; and a *hybrid* phase, characterized by the fuel ablation process. Both of them have been simulated in the code. Concerning the formulation of the first phase, the only difference with the hybrid one remains in the BL equations, where no flame nor source term in the mass balance equation are present.

In the simulation, the experimental measurements of the oxidizer mass flow and temperature at the exit of the catalyst are the inputs to the numerical domain. The evolution of their experimental measurements with time is represented in Fig. 8. The averaged pressure in the combustion chamber is imposed by the flow in the nozzle. To compute this pressure, the pseudo 2-D combustion chamber model has been coupled with the 1-D transient and compressible Euler equations in the nozzle, where the flow is assumed to be isentropic, with uniform properties across a section. A weight coefficient is used at the throat position in the nozzle through the evaluation of the Mach number at this point in an attempt to simulate the transition in the divergent part from a subsonic to a supersonic flow, thus allowing to avoid numerical instabilities when passing from one solution to the other.

Finally, the resulting thrust is calculated. On the basis of the values found by Durand [73] et al. for the HYCAT tests,

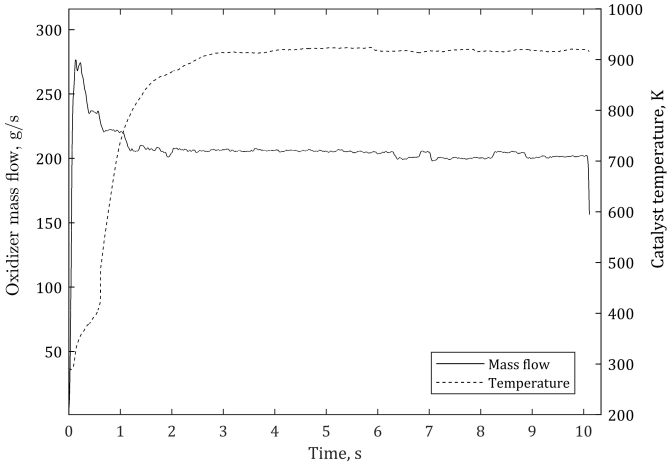

Fig. 8 Temporal evolution of the measured oxidizer mass flow and temperature at the exit of the catalytic injection and entering to the combustion chamber.

the combustion efficiency can be taken as $\eta_c = 0.89$. Thrust formulas are given by Eqs. (30)(a) and (30)(b).

$$\begin{cases} F = \eta_c c_F P_{ch} S_{th} & \text{(a)} \\ c_F = \sqrt{\left(\frac{2\gamma^2}{\gamma-1}\left(\frac{2}{\gamma+1}\right)^{\frac{\gamma+1}{\gamma-1}}\left[1-\left(\frac{P_{out}}{P_{ch}}\right)^{\frac{\gamma-1}{\gamma}}\right]\right)} + \frac{P_{out}-P_{amb}}{P_{ch}}\frac{S_{out}}{S_{th}} & \text{(b)} \end{cases} \tag{30}$$

A comparison between the temporal evolutions of the numerical and experimental space-averaged chamber pressure and thrust for the HYCAT 26 test are depicted in Figs. 9a and 9b. The experimental values have been smoothed following the moving average method in order to attenuate the measurement noise. The temporal changes in the spatial-averaged fuel regression rate and burnt thickness are represented in Fig. 9c. In all the figures, the non-reactive phase happening prior to the initiation of combustion is observed at the beginning of the test. To simulate this, it has been imposed that motor ignition and, therefore, fuel regression, begins when the temperature at the fuel surface of the first node of the chamber is superior to the fusion temperature of the solid fuel and when the gas temperature at the entrance is high enough to produce the reaction between the oxidizer and the pyrolyzed fuel gases. Our experiments have shown that when using a catalyst, the temperature measured at the exit of the catalytic injection that produces the initiation of fuel pyrolysis is of about 700-780 K, which is also close to the auto-ignition temperature of the main substance produced by the pyrolysis of the HDPE fuel (ranging from 720 to 760 K for the ethylene). By imposing T_{pyr} =700 K, a similar time duration of the non-reactive phase with respect to the experiment is found for HYCAT 26 (a numerical 0.92 s compared to the experimental 1 s). In this non-reactive phase, the growth of the averaged chamber pressure with time is related to the increase of the measured temperature at the exit of the catalyst. This pressure rises until reaching the corresponding choked-nozzle value in the nozzle, where the flow becomes supersonic in the divergent part.

Once combustion reaction happens, pressure in the chamber increases rapidly. During the transient regime in the hybrid phase, the numerical value of the regression rate increases too, just to decrease afterwards as a consequence of the oxidizer mass flux diminution (as studied in Sec. III.B), which is produced by the increase of the channel section, since the mass flow entering the chamber remains practically constant. In the hybrid phase, the slightly decrease of the pressure in the chamber with time is linked to the reduction in v_r: as flame temperature decreases with pressure [32], the heat flux transfers to the wall diminish too and consequently, a lower fuel consumption is retrieved. At the same time, the diminution of thrust with time is related to the decrease in pressure [see Eq. (30)]. In comparison with the experimental test, it has been observed that the computed values of pressure and thrust have been overestimated in average with respect to the measured ones. This fact is linked to the overestimation of the space-time averaged fuel regression rate value (see Table 2), which greatly influences the flow inside the nozzle and hence, the combustion chamber pressure (P_{ch}).

Figure 9d depicts the ratio of the local diameter by the initial diameter of the fuel block computed by the code for several instants from the beginning of the hybrid phase to the end of the test. The geometrical diameter of the fuel block measured at the end of the experiment at nine different axial positions is represented as well. The final diameter port shape provided by the computation is similar to the experimental one, with a 3.3% averaged of relative difference. Fuel consumption attains its highest value at the beginning of the channel, where skin friction is also larger. Then, it decreases along the axis, settling at a nearly constant value that increases slightly towards the end. This shape becomes slightly more pronounced as times passes and more fuel is consumed. The decreasing local fuel consumption trend observed along the first half of the port seems to correspond to the local continuous degressive tendency predicted by Marxman's theory [11], and employed in other authors' correlations [58, 74], where a maximum fuel pyrolysis at the entrance point is expected. Nonetheless, Carmicino and Sorge [72], employing an axial oxidizer injection, found in their experiments a concave fuel shape at the end of the burn. This result was due to the enhanced fuel consumption that is produced by the jet oxidizer impact on the fuel's surface. Moreover, the retrieved profile was more severe as the port diameter enlarged, deplacing downstream the position of maximum fuel regression. A concave v_r profile having a near-leading edge region with an accentuated fuel consumption associated to an existing recirculation flow has been found in other authors' HRE simulations [3, 4, 75]. However, the 1-D nature of our model does not allow us to simulate this 2-D effect related to the type of injection. Other experimental and numerical studies have found a similar local fuel consumption trend to the one retrieved from our simulation, meaning a high regression rate at the leading-edge of the chamber followed by a decrease in the consumption along the axial location until reaching a minimum value, beyond which the fuel regression rate started to increase [2, 57, 66, 76].

The numerical and experimental outcomes in HYCAT 12 and 23 tests dispay an equivalent behavior to the ones of HYCAT 26. A résumé of the computed averaged space-time pyrolysis rates and their relative discrepancies with the corresponding experimental values are shown in Table 2. Except for the HYCAT 12 test, where the discrepancies can attain 40%, the computed regression rates are thought to be a good estimation for the application of the developed combustion chamber model into a system design tool (errors under 30% required). However, despite the non-negligible overestimation of v_r for the HYCAT 12 test, the thrust force is found to be overestimated by 10% only over the experimental measurement for this test, which is still considered to be appropiate for the use of this model for an engine predesign code.

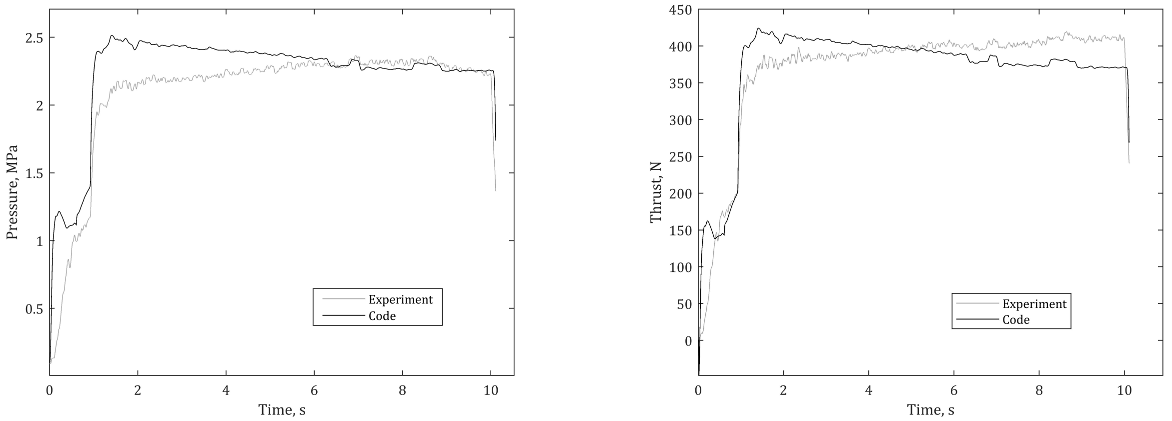

(a) Comparison of the experimental and numerical space-averaged chamber pressure evolution with time.

(b) Comparison of the experimental and numerical engine thrust evolution with time.

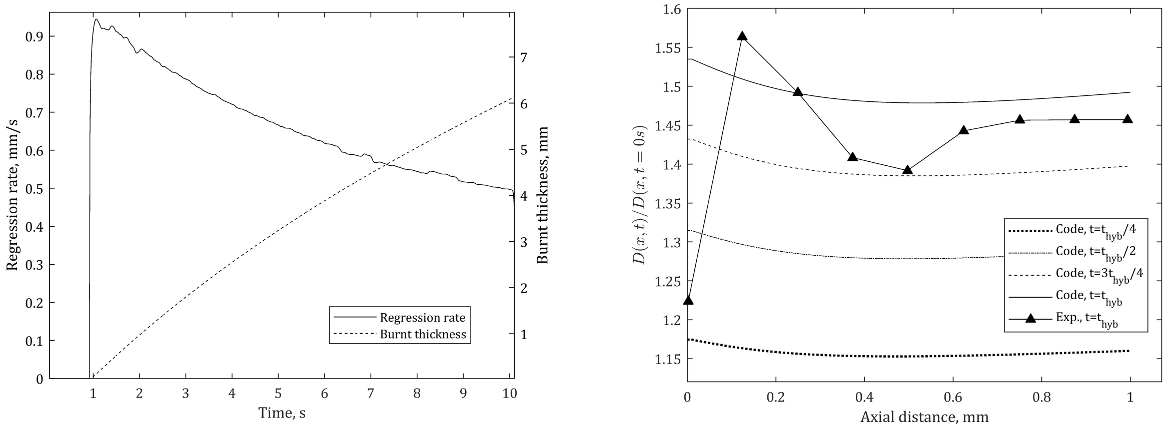

(c) Temporal evolution of the computed space-averaged fuel regression rate and burnt thickness.

(d) Comparison of the computed local diameters at several instants with the experimental solution at the end of the test.

Fig. 9 Numerical and experimental results for the HYCAT 26 test.

Table 2 Comparison of the experimental and numerical fuel regression rates for the HYCAT tests.

Test name	Experimental v_r (mm/s) [73]	Numerical v_r (mm/s)	Relative difference (%)
HYCAT 12	0.34 ± 0.03	0.472	39.9 ± 12.34
HYCAT 23	0.32 ± 0.02	0.393	23.29 ± 7.7
HYCAT 26	0.61 ± 0.05	0.669	10.41 ± 9.05

IV. Conclusion

An approximate 2-D modeling has been presented in this article using the integral core flow and BL axisymmetric equations, together with an Arrhenius law to describe the fuel pyrolysis in a cylindrical combustion chamber. Preliminary analysis have been performed in a non-reactive flow to check the capacity of the integral method to estimate the BL development, finding good agreements with the several BL characteristic thicknesses from literature. Then, several studies have been made with the purpose of verifying the implemented combustion and GSI models. For that, it has been evaluated whether the order of magnitude of the computed steady-state fuel regression rates for several mass fluxes and O/F couples is in agreement with the values provided by empirical v_r laws from literature. Despite the fact that the relative differences existing between the references and the results from the model can go from 3 to 51% when using some of these laws, the computed regression rates are found to be in the lower range of the reference v_r values for the different O/F couples analyzed. Nevertheless, during the comparison, we must keep in mind the dependence of the semiempirical v_r laws to the test conditions, the oxidizer injection type or the motor dimensions, which may result in a significant variation of their fit coefficients and hence, of the obtained v_r values from one author to another. In addition, from these studies, it has been proven the capacity of the pseudo 2-D model to correctly capture the impact of the oxidizer mass flux and the inner diameter of the fuel block on the regression rate values when compared with the references.

However, in order to actually assess the validity of this model to predict the HRE performances, a comparison with specific experimental tests must be done. For this, three tests performed at HYCAT (hybrid test bench of our laboratory) have been employed. An overestimation in the averaged fuel regression rate is found for all the three tests, producing, in average, between 10 to 40% of relative error. These discrepancies fall below 10% when comparing numerical and experimental values of thrust, chamber pressure or total ablated thickness. Nevertheless, to complete the validation process of the model presented in this article, more experimental tests (whose conditions can be simulated and applicable to our model) are thought to be necessary at higher mass fluxes and fuel block inner diameters to broaden and determine the limit of applicability of the model. Despite the fact that the discrepancies found in v_r between the simulations and the experiments may seem large, especially for the HYCAT 12 test, the obtained numerical results still remain encouraging for a future use of this combustion chamber model for the predesign phases of the engine, where errors under 30% are required. Indeed, our computations are performed quickly, taking only a few minutes of CPU time on a desktop computer to be completed. To sum up, and despite the errors, through the different validation analysis that have been carried out in this article, we have proven the capacity of an approximate 2-D HRE combustion chamber modeling to simulate the main elements affecting the fuel consumption and motor performances (engine thrust, chamber pressure) with time, obtaining in some cases a good estimation of these variables defining the HRE operation.

A numerical comparison of this model with the solution provided by the axisymmetric 2-D combustion chamber model of a HRE developed in the CFD tool of our laboratory (CEDRE) will be performed next as a means to evaluate the extent of the physics modeling of the pseudo 2-D code. After the completion of the numerical and experimental validation phases, we will perform the last necessary adjustments to improve the model and the provided results in views of its use for preliminary design phases of the HRE. If modifications are to be applied to the model, these will focus on the GSI and combustion models as they are thought to play a significant role in the computed value of v_r. Nonetheless, the use of correcting factors or the adjustment of the empirical laws that characterize the different coefficients appearing in the model (C_f, h_{conv}) or the velocity distribution over the BL, may allow a general improvement in the results without adding a great deal in the model complexity that would impact, thus, the computational time. Then, once the model is fixed and the final modifications are over, a sensitivity analysis will be carried out. The objective with this final study is to assess the influence of some factors, such as the aerodynamic parameters at the entrance of the channel (boundary layer initial thickness, oxidizer inlet temperature), the effect of the radiative heat over the energy transfers at the fuel surface, and the thermophysical properties specified for the fuel (density, specific heat, enthalpy of pyrolyzation), over the computed results, since a wide variety of these values is found in literature.

The final aim of this work is to integrate the developed model in our system design tool (currently under development) with the purpose of using it as a rapid predictive tool to estimate the HRE performances in preliminary design studies or to precede the preparation of experimental test campaigns. This tool could eventually implement an optimization algorithm allowing to find the best design solution for a HRE (couple of O/F, geometry and internal shape, inlet mass flow law, etc.) for some specified conditions (ΔV, spacecraft mass).

Funding Sources

This research has been supported by ONERA and CNES.

Acknowledgments

Special thanks to the Propulsion Laboratory Research Unit of the Fauga-Mauzac ONERA Centre for the realization of the experimental campaign on the HYCAT test bench.

References

[1] Carmicino, C., "Special Issue: Advances in Hybrid Rocket Technology and Related Analysis Methodologies," *Aerospace*, Vol. 6 (12), No. 128, 2019. https://doi.org/10.3390/aerospace6120128.

[2] Durand, J. E., Raynaud, F., Lestrade, J. Y., and Anthoine, J., "Turbulence Modeling Effects on Fuel Regression Rate in Hybrid Rocket Numerical Simulations," *Journal of Propulsion and Power*, Vol. 35, No. 6, 2019, pp. 1–16. https://doi.org/10.2514/1.B37528.

[3] Bianchi, D., Leccese, G., Nasuti, F., Onofri, M., and Carmicino, C., "Modeling of High Density Polyethylene Regression Rate in the Simulation of Hybrid Rocket Flowfields," *Aerospace*, Vol. 6, No. 88, 2019. https://doi.org/10.3390/aerospace6080088.

[4] Gallo, G., and Mungiguerra, S., "New Entrainment Model for Modelling the Regression Rate in Hybrid Rocket Engines," *Journal of Propulsion and Power*, Vol. 37, No. 6, 2021, pp. 893–909. https://doi.org/10.2514/1.B38333.

[5] Genevieve, B., Pitot, J., and Brooks, M., "A Computational Tool for Predicting Hybrid Rocket Motor Performance," *R&D Journal*, Vol. 33, 2017, pp. 56–65.

[6] Gieras, M., and Gorgeri, A., "Numerical Modelling of the Hybrid Rocket Engine Performance," *Propulsion and Power Research*, Vol. 10, No. 1, 2021, pp. 15–22. https://doi.org/10.1016/j.jppr.2021.03.001.

[7] Zolla, P., Migliorino, M., Bianchi, D., Nasuti, F., Pellegrini, R., and Cavallini, E., "A Computational Tool for the Design of Hybrid Rockets," *Aerotecnica Missili & Spazio*, Vol. 100, No. 4, 2021, pp. 387–397. https://doi.org/10.1007/s42496-021-00085-3.

[8] Jens, E., Cantwell, B., and Hubbard, G., "Hybrid Rocket Propulsion Systems for Outer Planet Exploration Missions," *Acta Astronautica*, Vol. 128, 2016, pp. 119–130. https://doi.org/10.1016/j.actaastro.2016.06.036.

[9] Casalino, L., and Pastrone, D., "Oxidizer Control and Optimal Design of Hybrid Rockets for Small Satellites," *Journal of Propulsion and Power*, Vol. 21, No. 2, 2005, pp. 230–238. https://doi.org/10.2514/1.6556.

[10] Mechentel, F., "Preliminary Design of a Hybrid Motor for Small-Satellite Propulsion," Ph.D. thesis, Dept. of Aeronautics and Astronautics, Stanford University, Stanford, CA, 2019.

[11] Marxman, G. A., "Combustion in the Turbulent Boundary Layer on a Vaporizing Surface," *Symposium (International) on Combustion*, Vol. 10, No. 1, 1965, pp. 1337–1349. https://doi.org/10.1016/S0082-0784(65)80268-5.

[12] Thwaites, B., "Approximate Calculation of the Laminar Boundary Layer," *The Aeronautical Quarterly*, Vol. 1, No. 3, 1949, pp. 245–280. https://doi.org/10.1017/S0001925900000184.

[13] Milewski, W., "Three-Dimensional Viscous Flow Computations Using the Integral Boundary Layer Equations Simultaneously Coupled with a low Order Panel Method," Ph.D. thesis, Dept. of Ocean Engineering, Massachusetts Inst. of Technology, Aug. 1997.

[14] Mughal, B., "Integral Method for Three-Dimensional Boundary-Layers," Ph.D. thesis, Dept. of Aeronautics and Astronautics, Massachusetts Inst. of Technology, 1998.

[15] Bayeux, C., Radenac, E., and Villedieu, P., "Theory and Validation of a 2D Finite-Volume Integral Boundary-Layer Method for Icing Applications," *AIAA Journal*, Vol. 57, No. 3, 2019, pp. 1092–1112. https://doi.org/10.2514/1.J057461.

[16] Lestrade, J., Anthoine, J., and Lavergne, G., "Liquefying Fuel Regression Rate Modeling in Hybrid Propulsion," *Aerospace Science and Technology*, Vol. 42, 2015, pp. 80–87. https://doi.org/10.1016/j.ast.2014.11.015.

[17] Wachs, A., Vinay, G., and Frigaard, I., "A 1.5D Numerical Model for the Start up of Weakly Compressible flow of a Viscoplastic and Thixotropic Fluid in Pipelines," *Journal of Non-Newtonian Fluid Mechanics*, Vol. 159, No. 1, 2009, pp. 81–94. https://doi.org/10.1016/j.jnnfm.2009.02.002.

[18] Amara, M., Capatina, D., and Lizaik, L., "Numerical Coupling of 2.5D Reservoir and 1.5D Wellbore Models in Order to Interpret Thermometrics," *International Journal for Numerical Methods in Fluids*, Vol. 56, No. 8, 2008, pp. 1115–1122. https://doi.org/10.1002/fld.1742.

[19] Pereira, T. M. D., and Uitenbroek, H., "RH 1.5D: a Massively Parallel code for Multi-Level Radiative Transfer with Partial Frequency Redistribution and Zeeman Polarisation," *Astronomy & Astrophysics*, Vol. 574, No. A3, 2015, pp. 1–6. https://doi.org/10.1051/0004-6361/201424785.

[20] Rohsenow, W. M., Hartnett, J. P., and Cho, Y. I., *Handbook of Heat Transfer*, 3$^{\text{rd}}$ ed., McGraw-Hill handbooks, McGraw-Hill Education, New York, 1998.

[21] Chung, M. Y., and Sung, H. J., "Spatial Simulation of the Instability of Channel flow with Local Suction/Blowing," *Physics of Fluids*, Vol. 9, No. 11, 1997, pp. 606–612. https://doi.org/10.1063/1.869423.

[22] Gordon, S., and McBride, B. J., "Computer Program for Calculation of Complex Chemical Equilibrium Compositions and Applications," *NASA reference publication 1311*, Oct. 1994.

[23] Barato, F., Lazzarin, M., Bellomo, N., Faenza, M., Bettella, A., and Pavarin, D., "A Numerical Model to Analyze Transient Behavior and Instabilities on Hybrid Rocket Motors," *47th AIAA/ASME/SAE/ASEE Joint Propulsion Conference & Exhibit*, AIAA Paper 2011-5538, San Diego, CA, July 2011. https://doi.org/10.2514/6.2011-5538.

[24] Serin, N., and Yalcin, G., "A Fast Computer Code for Hybrid Motor Design, Eulec, and Results Obtained for HTPB/O2 Combination," *39th AIAA/SME/SAE/ASEE Joint Propulsion Conference and Exhibit*, AIAA Paper 2003-4747, Huntsville, AL, 2003. https://doi.org/10.2514/6.2003-4747.

[25] Euler, L., "General principles concerning the motion of fluids - Principes généraux du mouvement des fluides," *Mémoires de l'Académie royale des sciences et des belles lettres de Berlin*, Vol. 11, 1957, pp. 274–315.

[26] Luxton, R., Bull, M., and Rajagopalan, S., "The Thick Turbulent Boundary Layer on a long fine Cylinder in Axial flow," *The Aeronautical Journal*, Vol. 88, No. 875, May 1984, pp. 186–199. https://doi.org/10.1017/S0001924000020480.

[27] Patel, V., "A Simple Integral Method for the Calculation of Thick Axisymmetric Turbulent Boundary Layers," Tech. Rep. IIHR Report No. 150, Iowa Institute of Hydraulic Research, University of Iowa, Iowa City, IA, Sept. 1973.

[28] Zilliac, G., and Karabeyoglu, A., "Hybrid Rocket Fuel Regression Rate Data and Modeling," *42nd AIAA/ASME/SAE/ASEE Joint Propulsion Conference & Exhibit*, AIAA Paper 2006-4504, Sacramento, CA, July 2006. https://doi.org/10.2514/6.2006-4504.

[29] Shah, R. K., and Bhatti, M. S., *Assessment of Correlations for Single-Phase Heat Exchangers*, Springer Netherlands, Dordrecht, 1988. https://doi.org/10.1007/978-94-009-2790-2_3.

[30] Zhi-qing, W., "Study on Correction Coefficients of Laminar and Turbulent Entrance Region Effect in Round pipe," *Applied Mathematics and Mechanics*, Vol. 3, 1982, pp. 433–446. https://doi.org/10.1007/BF01897224.

[31] Welty, J. R., Wicks, C. E., Wilson, R. E., and Rorrer, G. L., *Fundamentals Of Momentum, Heat, And Mass Transfer*, 5$^{\text{th}}$ ed., John Wiley & Sons, Inc., 2008.

[32] Helman, D., Wolfshtein, M., and Manheimer-Timnat, Y., "Theoretical Investigation of Hybrid Rocket Combustion by Numerical Methods," *Journal of Combustion and Flame*, Vol. 22, No. 2, 1974, pp. 171–190. https://doi.org/10.1016/S0010-2180(74)80004-0.

[33] Cai, G., and Tian, H., "Numerical Simulation of the Operation Process of a Hybrid Rocket Motor," *42nd AIAA/ASME/SAE/ASEE Joint Propulsion Conference & Exhibit*, AIAA Paper 2006-4506, Sacramento, CA, July 2006. https://doi.org/10.2514/6.2006-4506.

[34] Lazzarin, M., Barato, F., Pavarin, D., and Bettella, A., "CFD Simulation of Regression Rate in Hybrid Rockets," *Journal of Propulsion and Power*, Vol. 29, No. 6, 2013, pp. 1445–1452. https://doi.org/10.2514/1.B34910.

[35] Tian, H., Li, X., Zeng, P., Yu, N., and Cai, G., "Numerical and Experimental Studies of the Hybrid Rocket Motor with Multi-Port Fuel Grain," *Acta Astronautica*, Vol. 96, 2014, pp. 261–268. https://doi.org/10.1016/j.actaastro.2013.12.001.

[36] Chiaverini, M., Arves, J., Harting, G., Jones, H., Kuo, K. K., Lu, Y. C., Peretz, A., and Wygle, B., "Pyrolysis Behavior of Hybrid-Rocket Solid Fuels Under Rapid Heating Conditions," *Journal of Propulsion and Power*, Vol. 15, No. 6, 1999, pp. 888–895. https://doi.org/10.2514/2.5512.

[37] Lengellé, G., Fourest, B., Godon, J., and Guin, C., "Condensed-Phase Behavior and Ablation rate of Fuels for Hybrid Propulsion," *29th Joint Propulsion Conference and Exhibit*, AIAA Paper 93-2413, Monterey, CA, June 1993. https://doi.org/10.2514/6.1993-2413.

[38] Gascoin, N., Gillard, P., Mangeot, A., and Navarro-Rodriguez, A., "Literature Survey sor a First Choice of a Fuel-Oxidiser Couple for Hybrid Propulsion Based on Kinetic Justifications," *Journal of Analytical and Applied Pyrolysis*, Vol. 94, Nov. 2011, pp. 1–9. https://doi.org/10.1016/j.jaap.2011.11.006.

[39] Cherng, D., and Tao, C., "Analysis of Hybrid Rocket Combustion," *Acta Astronautica*, Vol. 7, No. 4, Apr.-May 1980, pp. 619–631. https://doi.org/10.1016/0094-5765(80)90049-1.

[40] Refloch, A., Courbet, B., Murrone, A., Villedieu, P., Laurent, C., Gilbank, P., Troyes, J., Tesse, L., Chaineray, G., Dargaud, J., Quémerais, E., and Vuillot, F., "CEDRE Software," *AerospaceLab Journal*, , No. AL02-11, 2011.

[41] Bassi, F., Botti, L., Verzeroli, L., Hartmann, R., Jägersküpper, J., Martin, E., Lorteau, M., Vincent, P., Witherden, F., Vermeire, B. C., Park, J., Iyer, A., Puri, K., Gutzwiller, D., Hirsch, C., and Chalot, F., *TILDA: Towards Industrial LES/DNS in Aeronautics*, Springer International Publishing, Cham, 2021, Chaps. Parallelisation to Several Tens-of-Thousands of Cores, pp. 259–319. https://doi.org/10.1007/978-3-030-62048-6_8.

[42] Schetz, J. A., *Boundary Layer Analysis*, Prentice Hall, New Jersey, 1993.

[43] Balsius, H., "Boundary Layers in Liquids with low Friction - Grenzschichten in Flüssigkeiten mit kleiner Reibung," *Journal of Applied Mathematics and Physics*, Vol. 56, 1908, pp. 1–37.

[44] Prandtl, L., *Results of the Aerodynamic Research Institute in Göttingen - Ergebnisse der Aerodynamischen Versuchsanstalt zu Göttingen Lfg. 3*, Oldebbourg Wissenschaftsverlag, Berlin, 1927. https://doi.org/10.1515/9783486755664.

[45] Simpson, R., Moffat, R., and Kays, W., "The Turbulent Boundary Layer on a Porous Plate: Experimental skin Friction with Variable Injection and Suction," *International Journal of Heat and Mass Transfer*, Vol. 12, No. 7, 1969, pp. 771–789. https://doi.org/10.1016/0017-9310(69)90181-1.

[46] Schetz, J. A., and Favin, S., "Numerical Calculation of Turbulent Boundary Layers Including Suction or Injection with Binary Diffusion," *Astronautica Acta*, Vol. 16, No. 6, 1971, pp. 339–352.

[47] Whitfield, D. L., "Integral Solution of Compressible Turbulent Boundary Layers using Improved Velocity Profiles," Tech. Rep. AEDC-TR-78-42, ARO, Inc., Arnold Air Force Station, TN, Dec. 1978.

[48] L. Pasiuk, S. M. H., and Chatham, R., "Experimental Reynolds Analogy Factor for a Compressible Turbulent Boundary Layer with a Pressure Gradient," Tech. Rep. NOL TR-64-200, U.S. Naval Ordnance Laboratory, White Oak, MD, Nov. 1964.

[49] Yu, Y., "Effect of Transverse Curvature on Turbulent-Boundary-Layer Characteristics," *Journal of Ship Research*, Vol. 2, No. 4, Dec. 1958, pp. 33–51. https://doi.org/10.5957/jsr.1958.2.4.33.

[50] Marxman, G. A., and Gilbert, M., "Turbulent Boundary Layer Combustion in the Hybrid Rocket," *Symposium (International) on Combustion*, Vol. 9, No. 1, 1963, pp. 371–383. https://doi.org/10.1016/S0082-0784(63)80046-6.

[51] Chiaverini, M., Harting, G., Kuo, K. K., and Peretz, A., "Regression Rate and Heat Transfer Correlations for Hybrid Rocket Combustion," *Journal of Propulsion and Power*, Vol. 17, No. 1, 2001, pp. 99–110. https://doi.org/10.2514/2.5714.

[52] Ito, S., Kamps, L., and Nagata, H., "Fuel Regression Characteristics in Hybrid Rockets Using Nitrous Oxide/High-Density Polyethylene," *Journal of Propulsion and Power*, Vol. 37, No. 2, March 2021, pp. 342–348. https://doi.org/10.2514/1.B37875.

[53] Carmicino, C., and Sorge, A., "Role of Injection in Hybrid Rockets Regression Rate Behaviour," *Journal of Propulsion and Power*, Vol. 21, 2005, pp. 606–612. https://doi.org/10.2514/1.9945.

[54] Sutton, G. P., and Biblarz, O., *Rocket Propulsion Elements*, 7th ed., John Wiley & Sons, New York, 2001.

[55] Frederick, R., Whitehead, J., Knox, L., and Moser, M., "Regression Rate Study of Mixed Hybrid Propellants," *Journal of Propulsion and Power*, Vol. 23, No. 1, 2007, pp. 175–180. https://doi.org/10.2514/1.14327.

[56] Shanks, R., and Hudson, M., "The Design and Control of a Labscale Hybrid Rocket Facility for Spectroscopy Studies," *30th Joint Propulsion Conference & Exhibit*, AIAA Paper 1994-3016, Indianapolis, IN, June 1994. https://doi.org/10.2514/6.1994-3016.

[57] George, P., Krishnan, S., Ramachandran, L., Ravindran, M., and Varkey, M., "Fuel Regression Rate in Hydroxyl-Terminated-Polybutadiene/Gaseous-Oxygen Hybrid Rocket Motors," *Journal of Propulsion and Power*, Vol. 17, No. 1, 2001, pp. 35–42. https://doi.org/10.2514/2.5704.

[58] Estey, P., Altman, D., and McFarlane, J., "An Evaluation of Scaling Effects for Hybrid Rocket Motors," *27th Joint Propulsion Conference*, AIAA Paper 1991-2517, Sacramento, CA, June 1991. https://doi.org/10.2514/6.1991-2517.

[59] Merotto, L., Boiocchi, M., Mazzetti, A., Maggi, F., Galfetti, L., and Luca, L. D., "Characterization of a Family of Paraffin-Based Solid Fuels," *4th European Conference for Aeronautics and Space Sciences*, EUCASS, St. Petersburg, Russia, July 2011.

[60] Risha, G., Evans, B., Boyer, E., Wehrman, R., and Kuo, K., "Nano-Sized Aluminium -and Boron- Solid-fuel Characterization in a Hybrid Rocket Engine," *39th AIAA/ASME/SAE/ASEE Joint Propulsion Conference and Exhbit*, AIAA Paper 2003-4593, Huntsville, AL, July 2003. https://doi.org/10.2514/6.2003-4593.

[61] Doran, E., Dyer, J., Lohner, K., Dunn, Z., Cantwell, B., and Zilliac, G., "Nitrous Oxide Hybrid Rocket Motor Fuel Regression Rate Characterization," *43rd Joint Propulsion Conference & Exhibit*, AIAA Paper 2007-5352, Cincinnati, OH, July 2007. https://doi.org/10.2514/6.2007-5352.

[62] Kim, S., Lee, J., Moon, H., Kim, J., Sung, H., and Kwon, O., "Regression Characteristics of the Cylindrical Multiport Grain in Hybrid Rockets," *Journal of Propulsion and Power*, Vol. 29, No. 3, 2013, pp. 573–581. https://doi.org/10.2514/1.B34619.

[63] Farbar, E., Louwers, J., and Kaya, T., "Investigation of Metallized and Nonmetallized Hydroxyl Terminated Polybutadiene/Hydrogen Peroxide Hybrid Rockets," *Journal of Propulsion and Power*, Vol. 23, No. 2, 2007, pp. 476–486. https://doi.org/10.2514/1.22091.

[64] Cai, G., Zeng, P., Li, X., Tian, H., and Yu, N., "Scale Effect of fuel Regression rate in Hybrid Rocket Motor," *Aerospace Science and Technology*, Vol. 24, No. 1, 2013, pp. 141–146. https://doi.org/10.1016/j.ast.2011.11.001.

[65] Chiaverini, M. J., and Kuo, K. K., *Fundamentals of Hybrid Rocket Combustion and Propulsion*, Progress in Astronautics and Aeronautics, Vol. 218, AIAA, Reston, 2007.

[66] Chiaverini, M., Johnson, D., Kuo, K. K., Lu, Y. C., Risha, G., and Serin, N., "Regression Rate Behavior of Hybrid Rocket Solid Fuels," *Journal of Propulsion and Power*, Vol. 16, No. 1, 2000, pp. 125–132. https://doi.org/10.2514/2.5541.

[67] Strand, L., Jones, M., Ray, R., and Cohen, N., "Characterization of Hybrid Rocket Internal Heat flux and HTPB fuel Pyrolysis," *30th Joint Propulsion Conference & Exhibit*, AIAA Paper 1994-2876, Indianapolis, IN, June 1994. https://doi.org/10.2514/6.1994-2876.

[68] Favarò, F., Manzoni, M., Coronetti, A., DeLuca, L., and William, S., "Solid Fuel Regression Rate Modeling for Hybrid Rockets," *Journal of Propulsion and Power*, Vol. 29, No. 1, Jan. 2013, pp. 205–215.

[69] Smoot, L. D., and Price, C. F., "Pressure Dependence of Hybrid fuel Regression Rates," *AIAA Journal*, Vol. 5, No. 1, 1967, pp. 102–106. https://doi.org/10.2514/3.3914.

[70] Knuth, W., Chiaverini, M., Gramer, D., and Sauer, J., "Solid-Fuel Regression Rate Behavior of Vortex Hybrid Rocket Engines," *Journal of Propulsion and Power*, Vol. 18, No. 3, June 2002, pp. 600–609. https://doi.org/10.2514/2.5974.

[71] Kumar, C. P., and Kumar, A., “Effect of Diaphragms on Regression Rate in Hybrid Rocket Motors,” *Journal of Propulsion and Power*, Vol. 29, No. 3, 2013, p. 559–572. https://doi.org/10.2514/1.B34671.

[72] Carmicino, C., and Sorge, A., “Influence of a Conical Axial Injector on Hybrid Rocket Performance,” *Journal of Propulsion and Power*, Vol. 22, No. 5, 2006, pp. 984–995. https://doi.org/10.2514/1.19528.

[73] Durand, J. E., Lestrade, J. Y., and Anthoine, J., “Restitution Methodology for Space and Time dependent Solid-Fuel Port Diameter Evolution in Hybrid Rocket Engines,” *Aerospace Science and Technology*, Vol. 110, 2021, p. 106497. https://doi.org/10.1016/j.ast.2021.106497.

[74] Karabeyoglu, A., Zilliac, G., and Cantwell, B., “Development of Scalable Space–Time Averaged Regression Rate Expressions for Hybrid Rockets,” *Journal of Propulsion and Power*, Vol. 23, No. 4, 2007, pp. 737–747. https://doi.org/10.2514/1.19226.

[75] Sanders, I., Bendana, F., Hagström, C., and Spearrin, R. M., “Injector Effects on Hybrid Polymethylmethacrylate Combustion Assessed by Thermochemical Tomography,” *Journal of Propulsion and Power*, Vol. 37, No. 6, 2021, pp. 928–943. https://doi.org/10.2514/1.B38316.

[76] Gariani, G., Maggi, F., and Galfetti, L., “Numerical Simulation of HTPB Combustion in a 2D Hybrid slab Combustor,” *Acta Astronautica*, Vol. 69, 2011, pp. 289–296. https://doi.org/10.1016/j.actaastro.2011.03.015.